

# The non-classical regime of the two-dimensional long-range XY model: a comprehensive Monte Carlo study

Dingyun Yao,<sup>1,\*</sup> Tianning Xiao,<sup>1,\*</sup> Chao Zhang,<sup>1,2,†</sup> Youjin Deng,<sup>1,3,4,‡</sup> and Zhijie Fan<sup>1,3,4,§</sup>

<sup>1</sup>*Hefei National Research Center for Physical Sciences at the Microscale and School of Physical Sciences, University of Science and Technology of China, Hefei 230026, China*

<sup>2</sup>*Department of Physics, Anhui Normal University, Wuhu, Anhui 241000, China*

<sup>3</sup>*Hefei National Laboratory, University of Science and Technology of China, Hefei 230088, China*

<sup>4</sup>*Shanghai Research Center for Quantum Science and CAS Center for Excellence in Quantum Information and Quantum Physics, University of Science and Technology of China, Shanghai 201315, China*

The interplay between short-range (SR) and long-range (LR) universal behaviors remains a fundamental topic in studying long-range interacting systems. The interaction between LR coupling and the Berezinskii-Kosterlitz-Thouless (BKT) mechanism introduces significant complexity, especially in the two-dimensional (2D) XY model, which is crucial for exploring low-dimensional phenomena and their implications for quantum computation. In the paper [arXiv:2404.08498], we investigated the 2D XY model with algebraically decaying interactions of the form  $1/r^{2+\sigma}$ . Our findings demonstrated continuous phase transitions into a ferromagnetic phase for  $\sigma \leq 2$ , characterized by the emergence of long-range order. In the ferromagnetic phase, for  $\sigma < 2$ , we identified a power-law decaying correlation function attributed to the Goldstone mode, and for  $\sigma = 2$ , logarithmic behaviors were observed. In this supplemental paper, we provide a comprehensive explanation of the detailed methodology, additional simulation results, and further insights into the above phenomena. It enhances our understanding of the crossover between SR and LR behaviors and has practical implications for experimental systems, such as Rydberg atom arrays.

## I. INTRODUCTION

Long-range (LR) interactions are prevalent in various natural phenomena, such as gravitational interactions between celestial bodies and electromagnetic interactions between particles. A key characteristic of these interactions is that their strength decays with distance according to a power-law. Introducing LR interactions into complex many-body systems can significantly influence their phase transition properties, leading to a richer array of physical phenomena. The first study of LR interactions dates back to 1969, when Dyson investigated their effects in a one-dimensional (1D) Ising chain by introducing the interaction term  $J_{ij} = |i - j|^{-(1+\sigma)}$  [1]. Dyson's work revealed that, unlike the original Ising model, which exhibited no phase transitions, the LR interactions induce a second-order phase transition at finite temperatures for  $0 < \sigma < 1$ . This finding underscores the profound impact of LR interactions on phase transitions, demonstrating that they can lead to new and interesting physical behaviors in many-body systems.

Upon this foundational work, the Ising model can be extended to the general  $O(\mathcal{N})$  model with LR interactions, where the interaction decays as  $r_{ij}^{-(d+\sigma)}$ . In this context,  $r_{ij}$  represents the distance between sites  $i$  and  $j$ , and  $d$  is the spatial dimension. This extension provides

a broader framework for understanding the effects of LR interactions in various many-body systems.

The long-range (LR)  $O(\mathcal{N})$  model was first thoroughly studied by Fisher using a renormalization group (RG) approach [2]. He categorized the system's behavior into three regimes based on the parameter  $\sigma$ : (1)  $0 < \sigma < \frac{d}{2}$  (classical regime): within this regime, the critical behavior of the system is governed by Gaussian fixed points; (2)  $\frac{d}{2} < \sigma < 2$  (non-classical regime): Gaussian fixed points cease to be stable, and the critical exponents vary with  $\sigma$ , with the critical exponent  $\eta$  posited to precisely retain its value within the mean-field regime, namely  $\eta = 2 - \sigma$ ; (3)  $\sigma > 2$  (short-range (SR) regime): in this interval, LR terms in the Hamiltonian become irrelevant, leading to the recovery of SR behavior. The regimes (1) and (3) have gained widespread acceptance, while regime (2) presents some issues. Firstly, the 1D LR Ising model undergoes a second-order phase transition for  $0 < \sigma < 1$  [1], a BKT transition at  $\sigma = 1$  [3, 4], and exhibits no phase transition for  $\sigma > 1$ , contradicting regime (2). Secondly, according to the regime (2), the exponent  $\eta$  might exhibit a sudden jump from 0 to  $\eta_{SR}$  at  $\sigma = 2$ , where  $\eta_{SR}$  denotes the  $\eta$  value under short-range interactions, which is perplexing. Later, Sak proposed an alternative framework, known as the "Sak's criterion", where the boundary between the non-classical and short-range regimes shifts from 2 to  $\sigma_* = 2 - \eta_{SR}$ . In this revised framework,  $\eta = 2 - \sigma$  is retained in the interval  $1 < \sigma < \sigma_*$ , and  $\eta = \eta_{SR}$  for  $\sigma > \sigma_*$ , thus simplifying  $\eta$  to  $\eta = \max(2 - \sigma, \eta_{SR})$ , eliminating the abrupt change in the exponent  $\eta$ . Sak's criterion has been supported by a series of theoretical and numerical works [5–10].

However, later Monte Carlo (MC) results with higher

\* These two authors contributed equally to this work

† chaozhang@ahnu.edu.cn

‡ yjdeng@ustc.edu.cn

§ zfanac@ustc.edu.cn

precision and subsequent theoretical work suggest a different picture, where  $\eta$  transitions smoothly from  $2 - \sigma$  near  $\sigma = 1$  to  $\eta_{SR}$  at  $\sigma = 2$ , and the threshold  $\sigma_*$  returns to 2 [11, 12]. Additionally, another MC study of a percolation model with LR probabilities seems to agree with this picture [13]. Later, another numerical study indicated the possible existence of double power in the correlation function near  $\sigma = 2 - \eta_{SR}$ , attributing this deviation to an underestimation of finite-size corrections [9].

Overall, Sak's criterion has achieved considerable recognition, but some controversies persist. Most numerical validations have been confined to the 2D LR Ising model, with limited exploration of LR  $O(\mathcal{N})$  models for  $\mathcal{N} \geq 2$ . For instance, Ref.[14] studied the XY model on a 2D complex topology, which is expected to belong to the same universality class as the 2D LR XY model. Similarly, Ref.[15] investigated the 2D LR Heisenberg model. However, these studies did not focus on determining the threshold point  $\sigma_*$ , and their simulations were limited to relatively small system sizes, with a maximum length of only 256. Therefore, there is a pressing need for a more detailed numerical study of these models.

Additionally, the phase diagrams of the 2D LR XY model may exhibit unique characteristics worth exploring. The 2D XY model is known to undergo a BKT transition [3] with an exponent  $\eta = 0.25$ , transitioning into a low-temperature phase with quasi-long-range order (QLRO). Previous studies have shown that the 2D LR XY model displays spontaneous magnetization at low temperatures for  $\sigma < 2$  [16]. This suggests that if Sak's criterion holds for the 2D LR XY model, then within the interval  $2 - \eta_{SR} = 1.75 < \sigma < 2$ , the system should exhibit both a BKT transition and a low-temperature ferromagnetic phase. This scenario is particularly intriguing — recent work by Refs. [17, 18] has proposed a phase diagram where the LR XY system exhibits two phase transitions for  $1.75 < \sigma < 2$ : first a BKT transition into a QLRO phase, followed by a second-order transition into a ferromagnetic phase. Thus, a thorough and careful numerical investigation into whether the special phase diagram indeed exists is both necessary and meaningful.

This paper is the accompanying paper of our previous work [19] to enhance further the understanding of the physics of the 2D LR XY model. In particular, we study the model via large-scale Monte Carlo (MC) simulations with the largest system size reaching  $L = 8192$ . Instead of further refining the estimate of critical exponents in the non-classical regime, we focus on both the low-temperature and high-temperature properties of the model [19]. Our phase diagram for the LR XY model is shown in Figure 1. For  $\sigma > 2$ , the system displays SR behavior: a BKT transition to QLRO for the XY model. For  $\sigma < 2$ , the system exhibits a second-order phase transition, with critical exponents varying according to  $\sigma$ . In our research, we present a series of evidence that clearly indicates that the threshold between LR and SR universality is at  $\sigma_* = 2$  for the 2D LR XY model, which is inconsistent with Sak's scenario and the proposed phase

diagram in Ref. [17, 18].

1. The second-moment correlation length ratio  $\xi/L$  (will be defined in the later section) is a powerful tool for identifying the transition type and the critical point. Specifically, for a second-order transition,  $\xi/L$  curves for different  $L$ s intersect at the critical point and diverge in the low- $T$  phases as  $L$  increases. In contrast, for a BKT transition,  $\xi/L$  curves for different  $L$ s converge to a smooth function in the QLRO phase. Our results show that for  $\sigma \leq 2$ , the scaling behavior of  $\xi/L$  is consistent with the second-order transition, while for  $\sigma > 2$ , typical BKT physics is observed.

2. In the low- $T$  phases, we demonstrate that, for  $\sigma \leq 2$ , the system exhibits long-range ferromagnetic order in the thermodynamic limit, while for  $\sigma > 2$ , the system enters a QLRO phase. In addition, the spontaneous symmetry breaking for  $\sigma < 2$  leads to Goldstone mode excitations, which give rise to a correlation function that decays algebraically to a constant, as  $g(x) \sim x^{-\eta_\ell} + g_0$ . Here, the anomalous dimension  $\eta_\ell = 2 - \sigma$  is theoretically derived and confirmed numerically. Moreover, for the marginal case of  $\sigma = 2$ , where theoretical derivation is absent, logarithmic behavior is observed in the low- $T$  phase.

3. In the high- $T$  phases, as  $T$  decreases to the critical point  $T_c$ , the growth behaviors of  $\xi$  for  $\sigma \leq 2$  and  $\sigma > 2$  are drastically different. For  $\sigma > 2$ , typical BKT behavior is observed,  $\xi \sim \exp(b/\sqrt{t})$ , where  $t = (T - T_c)/T_c$  is the reduced temperature and  $b$  is some non-universal constant. However, for  $\sigma \leq 2$ , the growth of  $\xi$  increasingly deviates from the BKT behavior as  $t \rightarrow 0$ . It asymptotically follows the power-law divergences of a second-order transition as  $\xi \sim t^{-\nu}$ , where  $\nu$  is the critical exponent of the correlation length.

4. Based on the previous knowledge of transition type, we carefully determine the critical temperature and critical exponents of the transitions for  $\sigma \leq 2$ . Our results do not support Sak's scenario. Specifically, the anomalous dimension varies continuously in the regime  $1 < \sigma \leq 2$ .

In this auxiliary paper, we offer a more comprehensive explanation of our work, including the methodology, detailed analysis of the simulation results, and further insights to enhance our previous findings. In the following sections, we first describe the model and present the enhanced MC algorithm in Section II. The observables measured and their finite-size scaling analysis are also included. Sections III-VI then provide detailed results and analysis, including an overall explanation of the system at various  $\sigma$ , the low-temperature properties, high-temperature properties, and the critical point along with critical exponents. Finally, we summarize our findings in Section VII.

## II. MODEL, ALGORITHM, AND OBSERVABLES

### A. Model

In this work, we investigate the LR XY model on a two-dimensional (2D) square lattice with periodic boundary conditions (PBC). The Hamiltonian of the model is given by,

$$\mathcal{H} = - \sum_{i < j}^N J_{ij} \mathbf{S}_i \cdot \mathbf{S}_j, \quad (1)$$

where  $\mathbf{S}_i$  is a two-component unit vector corresponding to the XY spin at the  $i$ -th site, and  $N = L \times L$  is the total number of spins with  $L$  being the linear system size. The lattice spacing is set to unitary. The summation in Eq. (1) runs over all spin pairs, and the total number of interaction terms is  $N_b = N(N-1)/2$ . The spins interact with each other via an algebraically decaying ferromagnetic coupling,

$$J_{ij} = \frac{J}{|\vec{r}_i - \vec{r}_j|^{2+\sigma}}, \quad (2)$$

where  $J = 1$  is the coupling constant, and  $\vec{r}_i$  is the coordinate of the  $i$ -th site on the square lattice. In the  $\sigma \rightarrow \infty$  limit, the model reduces to the nearest-neighbor (NN) XY model, which enters a quasi-long-range order phase at low- $T$  through the celebrated BKT transition [3]. In the  $\sigma \rightarrow -2$  limit, this model becomes the XY model on a complete graph (CG), corresponding to the infinite-dimensional lattice with PBC in the thermodynamic limit [20–22]. In this work, we focus on the  $\sigma > 0$  regime, where the energy is strictly extensive, i.e., the energy density of the system remains finite in the thermodynamic limit.

To properly account for the long-range interactions across the periodic boundaries, the minimum-image convention is utilized [23–25]. The square lattice with PBC maps onto a torus, and spins interact via the shortest distance on the surface of the torus. Specifically, let  $\vec{r}_{ij}$  being the displacement vector between sites  $i$  and  $j$ , the  $\alpha = x, y$  component of  $\vec{r}_{ij}$  is calculated as,

$$r_{ij}^\alpha = \begin{cases} r_j^\alpha - r_i^\alpha - L/2, & \text{if } r_j^\alpha - r_i^\alpha > +L/2 \\ r_j^\alpha - r_i^\alpha + L/2, & \text{if } r_j^\alpha - r_i^\alpha < -L/2 \\ r_j^\alpha - r_i^\alpha, & \text{otherwise} \end{cases}. \quad (3)$$

In this model, the interaction range is not artificially truncated, and each spin interacts with all other  $N-1$  spins.

The long-range interaction makes the average energy scale of the system depend on  $\sigma$  and  $L$ , which can lead to a strong finite-size correction. To mitigate this correction and interpolate between the  $\sigma \rightarrow \infty$  and  $\sigma \rightarrow 0$  scenarios, we introduce a normalization constant  $c(\sigma, N)$  to the Hamiltonian (1) [26]. This normalization ensures

that for all  $\sigma > 0$  and  $L$ , the average coupling strength for each spin equals that of the NN case,

$$c(\sigma, N)^{-1} = \frac{1}{4J} \sum_{j=1}^{N-1} J_{0j}. \quad (4)$$

Hence, the long-range interaction strength  $J_{ij}$  becomes,

$$J_{ij} = c(\sigma, N) \frac{J}{|\vec{r}_i - \vec{r}_j|^{2+\sigma}}. \quad (5)$$

Although this normalization changes the averaged energy scale, it does not alter the algebraically decaying form of the interaction. Consequently, only the non-universal attributes of the phase transition, like the position of the critical points, are affected. The universal scaling properties at the critical point and the boundary between the LR and SR regimes remain unchanged. Hereafter, the interaction strength  $J_{ij}$  refers to the normalized version defined in Eq. (5).

Another convention to mitigate the finite-size effects in long-range interacting systems is the Ewald summation technique, where the coupling constant  $J_{ij}$  is modified to include the interactions of all periodic images of the system [8, 10]. This method is equivalent to our normalization treatment in the thermodynamic limit, only to differ in the finite-size correction terms to observables. For large-scale simulations, our method is more straightforward and asymptotically the same as the Ewald summation method in reducing the finite-size effect.

### B. Algorithm

Simulating long-range interactions using the Monte Carlo method presents two key challenges: the critical slowing-down near phase transitions and escalating simulation time with increasing system size. Critical slowing-down arises near the critical point, where consecutive samples become highly correlated. This correlation leads to a significant decrease in simulation efficiency as the system size increases. Various strategies have been developed to address this issue, such as cluster algorithms [27, 28], direct-loop algorithms [29], and worm algorithms [30]. The rapidly increasing simulation time is another major hurdle in accurately analyzing the critical properties of a long-range system. For a long-range interacting spin system of size  $N$ , each spin interacts with other  $N-1$  spins, so a proposed local MC update requires evaluating all  $N-1$  interaction terms. This results in a *computational complexity*  $\mathcal{C}$  of  $\mathcal{O}(N)$  for the LR system, compared to  $\mathcal{O}(1)$  for the NN case. Here, the computational complexity is defined as the average number of operations required to update a single spin, serving as a measure of the time complexity of the MC algorithm. In practice, the actual CPU time of an MC local update is proportional to  $\mathcal{C}$ . Several methods have been proposed to mitigate this challenge. Techniques such as the

worm algorithm combined with the diagrammatic Monte Carlo method expand the pairwise potential energy into diagrammatic contributions, making the computational complexity independent of system size [31]. Efficient cluster algorithms for the classical long-range Ising model have also been developed [32, 33]. The recently introduced clock Monte Carlo method [26, 34], based on the factorized Metropolis filter [35], reduces computational complexities of several classical LR models to  $\mathcal{O}(1)$ .

In this work, we simulate the LR XY model using an enhanced variant of the Luijten-Blöte (LB) algorithm [32, 36]. We augmented the original LB algorithm with the clock Monte Carlo method and extended it to the  $O(N)$  spin model. This approach employs the cluster updates scheme to address the issue of critical slowing down and adopts an efficient cluster construction strategy to reduce the computational complexity associated with long-range interactions. Without loss of generality, we elucidate the algorithm for the  $O(\mathcal{N})$  spin model with long-range interactions.

We begin with the standard multi-cluster algorithm for a long-range  $O(\mathcal{N})$  spin model. A Monte Carlo sweep consists of two main steps: cluster construction and cluster flipping. The cluster construction starts by randomly choosing a unit vector  $\mathbf{S}_{\text{ref}}$  in the  $\mathcal{N}$ -dimensional space. Each spin  $\mathbf{S}$  is projected onto this reference vector, yielding the parallel component  $S^{\parallel} = \mathbf{S} \cdot \mathbf{S}_{\text{ref}}$ . Spin clusters are then formed by sequentially inspecting all pairs of spins (bonds). Each bond  $(i, j)$  is independently activated with probability,

$$\rho_{ij} = \left[ 1 - e^{-2\beta J_{ij} S_i^{\parallel} S_j^{\parallel}} \right]^+, \quad (6)$$

with  $[x]^+ = \max(0, x)$ . After all the bonds have been examined, spins connected by active bonds form clusters, which are then independently flipped with probability 1/2. A flipped spin is given by  $\mathbf{S}' = \mathbf{S} - 2S^{\parallel} \mathbf{S}_{\text{ref}}$ . An updated configuration is generated after all clusters have been considered for flipping. The algorithm operates with a computational complexity of  $\mathcal{O}(N)$ , as each MC sweep involves evaluating  $N(N-1)/2$  bonds, and on average,  $\mathcal{O}(N)$  operations are required per spin.

In the 1990s, Luijten and Blöte introduced an efficient cluster algorithm for the long-range Ising model [32]. Their method is based on the observation that, on average, only  $O(N)$  among  $O(N^2)$  bonds participate in the cluster construction. They proposed a rejection-free approach using the binary search to directly sample the next bond to activate (the bond activation event) instead of sequentially inspecting all bonds. This strategy reduces the number of operations per MC sweep to  $O(N \log N)$ , resulting in a computational complexity of  $O(\log N)$ , which drastically increases the efficiency of the algorithm. Nevertheless, their method is primarily limited to the LR Ising model. Additionally, the binary search requires a look-up table to sample the bond activation events, making it technically challenging to apply to 2D models, and special modifications to the coupling

function are needed [8].

To overcome these limitations, we integrated the clock Monte Carlo method with the LB algorithm. The clock Monte Carlo method replaces the conventional Metropolis acceptance criterion with a factorized Metropolis filter — a product of independent factors where an update is rejected if any independent factor fails. By directly sampling the first rejecting factor (first-rejection event) using the clock sampling technique, the computational complexity is significantly reduced from  $O(N)$  to  $O(1)$ . Recognizing the similarity between first-rejection events and bond activation events, we apply the clock sampling technique to sample bond activation events efficiently.

Following the Ref [26], we first introduce a *configuration-independent* activation probability for each bond

$$\hat{\rho}_{ij} = 1 - e^{-2\beta J_{ij}}. \quad (7)$$

This probability depends solely on the strength of the interaction  $J_{ij}$  and ensures that for any spin configuration,  $\hat{\rho}_{ij} \geq \rho_{ij}$ . Hence,  $\hat{\rho}_{ij}$  is referred to as the *bound activation probability*. The actual activation of a bond  $(i, j)$  is then determined by first attempting a bound activation with probability  $\hat{\rho}_{ij}$ , followed by resampling with a relative probability:

$$\rho_{ij, \text{rel}} = \rho_{ij} / \hat{\rho}_{ij}. \quad (8)$$

Therefore, by introducing the bound activation probability and the resampling process, a bond inspection is only required when a bound acceptance occurs. We shall leverage this property for efficient sampling of bond activations.

In a long-range  $O(\mathcal{N})$  model, the bonds can be categorized into different types based on their displacement vector  $\vec{r}$  [37]. Each type of bond shares the same bound activation probability  $\hat{\rho}$ . To construct clusters, we first obtain, for each type of bond, a list of bonds that are bound activated. Then, these bound-activated bonds are resampled to inspect for actual activation. Such a list can be obtained by sampling the distribution  $P(k) = \hat{\rho}(1-\hat{\rho})^{k-1}$  which expresses the probability that the  $k$ -th bonds are bound activated, while  $k-1$  previous bonds are rejected and skipped. When the  $\hat{\rho}$  is small, which is the case near  $T_c$ , most bonds are skipped before a bond is inspected for activation. For a type of bond that consists of  $N_k$  bonds with  $\hat{\rho}$ , the bond activation process works as follows:

- (a) Initially, set index  $k = 0$ .
- (b) Calculate the index of the next bond to inspect using

$$k \leftarrow k + 1 + \left\lfloor \frac{\ln(r)}{\ln(1-\hat{\rho})} \right\rfloor, \quad (9)$$

where  $r$  is a uniform random number in  $(0, 1]$  and  $\lfloor x \rfloor$  denotes the floor function that returns the integer part of  $x$ .

- (c) If  $k \leq N_k$ , attempt to activate the  $k$ -th bond with relative probability  $\rho_{k, \text{rel}}$ .

(d) Repeat from step (b) until  $k > N_k$ .

The cluster construction process concludes once all types of bonds have been considered. This procedure leads to a considerably faster algorithm due to the reduced number of bond inspections and random number generation. Compared to the LB algorithm, our method eliminates the need for a look-up table and alleviates truncation errors associated with discrete cumulative probability integration approximations. It reproduces the stochastic dynamics of the original multi-cluster method while achieving a  $O(1)$  computational complexity within the parameter space studied in this work. In practice, care should be taken to avoid double-counting, which can be achieved by selecting unique displacement vectors on the torus.

We have performed extensive MC simulations of the LR XY model using the algorithm described in this subsection, with system sizes ranging from  $L = 16$  to  $L = 8192$ . Each system is thermalized for  $4 \times 10^3$  MC sweeps, which is sufficient to reach thermal equilibrium. For system sizes  $L \leq 4096$  at low temperatures  $\beta = 1, 2, 4, 8$  and near the critical temperature of various  $\sigma$ , we collect over  $2 \times 10^6$  samples to achieve high statistical accuracy. Under other parameters, where high-precise data is not required for fitting, the minimal number of samples is  $4 \times 10^5$ . Simulations for the largest system size  $L = 8196$  are conducted at selected parameters, and the results are obtained from over  $4 \times 10^4$  samples. Like other cluster algorithms, our simulation does not suffer from the critical-slowing down issue. Specifically, for a simulation with  $L = 8192$  and  $\sigma = 2$  near the critical point  $T_c$ , the integrated autocorrelation time  $\tau_{\text{int}}$  in the unit of MC sweep is  $\sim 9$  for the energy-like quantity and  $\sim 4.6$  for the squared magnetization. In this particular case, the average computational complexity is  $\sim 2$  operations per spin, which remains virtually constant for all simulations near  $T_c$  in this work, and it takes around 11 CPU days to go over  $10^4$  MC sweeps. Moreover, the CPU time per spin update is proportional to the computational complexity, and the space complexity of the algorithm scales linearly with system volume  $N$ . For the largest system size  $L = 8192$  simulated in this work, our implementation requires  $\sim 10.5$  Gigabyte of memory.

### C. Sampled Quantities

Various physical quantities are sampled in the simulation to investigate the properties of the model. After thermalization, the observables are measured after every MC sweep. For a given spin configuration, we sample the following observables:

- (a) Total energy from the NN interactions,  $\varepsilon = -J_{\text{nn}} \sum_{\langle i,j \rangle} \mathbf{S}_i \cdot \mathbf{S}_j$ , where  $\langle i,j \rangle$  denotes nearest neighboring pairs of spins and  $J_{\text{nn}} = c(\sigma, N)J$  is the NN coupling strength.
- (b) Magnetization density  $\mathbf{M} = L^{-2} \sum_{i=0}^N \mathbf{S}_i$ , and its

Fourier mode  $M_{\mathbf{k}} = L^{-2} |\sum_i \mathbf{S}_i e^{i\mathbf{k} \cdot \mathbf{r}_i}|$ , where  $\mathbf{k} = \frac{2\pi}{L} \hat{\mathbf{x}}$ , the smallest wave vector of the reciprocal lattice in  $\mathbf{x}$ -direction.

The measurement consumes only a small fraction of the total simulation time, which is almost negligible. We then obtain the ensemble average ( $\langle \cdot \rangle$ ) of the following quantities:

- (i) The magnetic susceptibility  $\chi = L^2 \langle M^2 \rangle$  and its Fourier mode  $\chi_k = L^2 \langle M_k^2 \rangle$ .
- (ii) The 2<sup>nd</sup>-moment correlation length [38–40], defined as

$$\xi_{2\text{nd}} = \frac{1}{2 \sin(|\mathbf{k}|/2)} \sqrt{\langle M^2 \rangle / \langle M_k^2 \rangle - 1}. \quad (10)$$

- (iii) The Binder ratio of magnetization

$$Q_m = \frac{\langle M^2 \rangle^2}{\langle M^4 \rangle} \quad (11)$$

- (iv) The scaled covariance between  $\varepsilon$  and  $M^2$ ,

$$K = -\frac{L^2}{\langle M^2 \rangle} (\langle \varepsilon M^2 \rangle - \langle \varepsilon \rangle \langle M^2 \rangle) \quad (12)$$

Note that the second-moment correlation length  $\xi_{2\text{nd}}$  is different from the commonly referred exponential correlation length  $\xi_{\text{exp}}$ . The former is defined based on the Fourier spectrum of the correlation function [39, 41], while the latter is obtained by fitting the exponentially decaying correlation function. Both correlation lengths are well-defined in the disordered phase and become asymptotically equivalent in the thermodynamic limit, sharing the same scaling behavior near the critical point. Compared to  $\xi_{\text{exp}}$ , the second-moment correlation  $\xi_{2\text{nd}}$  is much easier to measure in MC simulations. Conversely, obtaining  $\xi_{\text{exp}}$  can be challenging due to finite-size effects that complicate the fitting process. Hereafter, unless specified otherwise, the correlation length  $\xi$  refers to the second-moment correlation length.

Furthermore, the dimensionless ratio  $\xi/L$  is an effective tool for identifying the critical points of phase transitions [40, 42, 43]. At criticality, quantity  $\xi/L$  attains a universal value in the thermodynamic limit. In the disordered phase, where the correlation length  $\xi$  is finite, this ratio drops to zero as the system size  $L$  increases. In contrast, in the ordered phase,  $\xi/L$  diverges rapidly because  $M^2$  remains finite while  $M_k^2$  vanishes quickly with increasing  $L$ . For a second-order transition, the intersection of  $\xi/L$  curves for different  $L$  accurately pinpoints the critical point. In the case of a BKT transition, however, the ratio converges to a universal curve in the QLRO phase.

Throughout the simulation, the error bars are estimated using standard error analysis techniques: for simple observables, such as  $\varepsilon$ ,  $M^2$ , and  $M_k^2$ , the error bars

are calculated using the standard binning method; for composite observables obtained by the arithmetic combinations of simple observables, such as the 2nd-moment correlation length  $\xi$  and Binder ratio  $Q$ , the error bars are estimated using the jackknife method.

#### D. Finite-size Scaling Analysis

Finite-size scaling (FSS) analysis is an essential technique in the numerical investigation of critical phenomena. In the language of the renormalization group (RG), the critical behavior of systems belonging to the same universality class is governed by a common fixed point. Near critical points, the free energy, and thus other physical observables, can be expressed as universal functions of scaling fields. FSS extends these universal functions to finite systems, enabling precise determination of critical points and accurate extraction of critical exponents. Near the critical point, the free-energy density  $f(t, h, u, L^{-1})$  is a function of the thermal scaling field  $t$ , the magnetic scaling field  $h$ , an irrelevant field  $u$ , and the finite-size field  $L^{-1}$ . Then, the FSS behavior of free-energy density is given by,

$$f(t, h, u, L^{-1}) = L^{-d} f(tL^{y_t}, hL^{y_h}, uL^{y_u}, 1) + g(t, h), \quad (13)$$

where  $y_t$ ,  $y_h$  and  $y_u$  are the corresponding scaling exponent and  $g$  is the analytic part of free-energy density. The scaling fields are non-universal functions of microscopic interactions and external physical parameters. To the lowest order,  $t$  is proportional to  $T - T_c$ , i.e., the distance between temperature and critical temperature;  $h$  is proportional to the physical external magnetic field  $H$ . The irrelevant field  $u$  reflects the distance of criticality of the system and the fixed point.

The FSS behavior of various physical observables near  $T_c$  can be derived from Eq. (13). Here, we present the scaling form of several key quantities near or at a second-order phase transition: (a) magnetic susceptibility  $\chi$ , (b) scaled covariance  $K$ , and (c) dimensionless quantities, such as  $Q_m$  and  $\xi/L$ .

**(a) Scaling behavior of  $\chi$ .** The magnetic susceptibility  $\chi$  is calculated from the averaged squared magnetization  $\langle M^2 \rangle$ , which is proportional to  $\partial^2 f / \partial h^2$  at  $h = 0$ . Thus, near the critical point, the magnetic susceptibility scales as

$$\chi = L^{2y_h - d} \tilde{\chi}(L^{y_t} t, L^{y_u} u, 1) + \dots, \quad (14)$$

where  $\tilde{\chi}$  is a universal function, and the contribution due to  $g$  is not specified. The leading exponent  $2y_h - d$  can be replaced by  $2 - \eta$  where  $\eta$  is the anomalous dimension of the correlation function at the critical point.

**(b) Scaling behavior of  $K$ .** The quantity  $K$  is proportional to the correlation between the squared magnetization  $M^2$  and the NN energy  $\varepsilon$ . The NN energy  $\varepsilon$  shares a similar scaling behavior as the total energy  $E$

near  $T_c$  as  $\sim L^{y_t - d}$  [37, 44]. Consequently, the correlation between  $M^2$  and  $\varepsilon$  is proportional to the temperature derivative of squared magnetization  $\frac{\partial}{\partial t} \langle M^2 \rangle$  [37]. The FSS form of  $K$  at the critical point  $t = 0$  is then given by

$$K \propto \frac{1}{\langle M^2 \rangle} \frac{\partial}{\partial t} \langle M^2 \rangle \Big|_{t=0} = \frac{1}{\chi} \frac{\partial}{\partial t} \chi \Big|_{t=0} \quad (15)$$

$$\approx a_0 L^{y_t} (1 + a_1 L^{y_u}) + a_2 L^{y_t + d - 2y_h} + \dots, \quad (16)$$

where  $a_i$  are non-universal constants. The leading  $L^{y_t}$  scaling behavior in Eq. (16) makes  $K$  an excellent quantity to estimate the thermal scaling exponent  $y_t$ .

**(c) Scaling behavior of dimensionless ratios.** Dimensionless ratios, such as Binder ratio  $Q_m$  and correlation length ratio  $\xi/L$ , have been widely used in FSS analysis to locate the critical point of phase transitions [42, 43, 45]. Near the critical point, the Binder ratio follows the scaling behavior

$$Q_m(t, u, L) = Q_m(tL^{y_t}, uL^{y_u}, 1) + \dots, \quad (17)$$

where the ellipsis denotes omitted correction terms arising from the field dependence of the analytic part of the free energy and higher-order contributions. Similarly, since the correlation length  $\xi$  scales as the system size  $L$  near  $T_c$ , the FSS form of correlation length ratio  $\xi/L$  is given by,

$$\xi/L \sim \tilde{\xi}(tL^{y_t}, uL^{y_u}, 1), \quad (18)$$

where  $\tilde{\xi}(\cdot)$  is a universal scaling function.

### III. RESULTS: OVERVIEW

Before delving into the detailed analysis of the LR XY model, we provide an overview of the main findings to facilitate a better understanding. As the long-range model enters the non-classical regime in  $\sigma \leq \sigma_*$ , the critical behavior differs from that of the short-range regime. For the LR Ising model, the universal properties of the transition, such as the critical exponents and other universal quantities, vary as  $\sigma$  in the non-classical regime. Therefore, previous studies of the LR Ising model focus on the accurate extraction of critical exponents or the scaling behavior of universal values, which, however, can be extremely subtle [8, 10, 11]. In contrast, for the LR XY model, we expect a much more evident signature when the system enters the non-classical regime — the type of transition changes from a BKT transition to a second-order transition. The change in transition type leads to drastically different behaviors in both the low-temperature and high-temperature phases and the critical points, making determining  $\sigma_*$  much easier than the LR Ising case.

Based on extensive MC simulations from our previous work [19] and the present study, we have identified three distinct regimes in the phase diagram of the LR XY model: the *classical* regime ( $\sigma \leq 1$ ), the *non-classical*

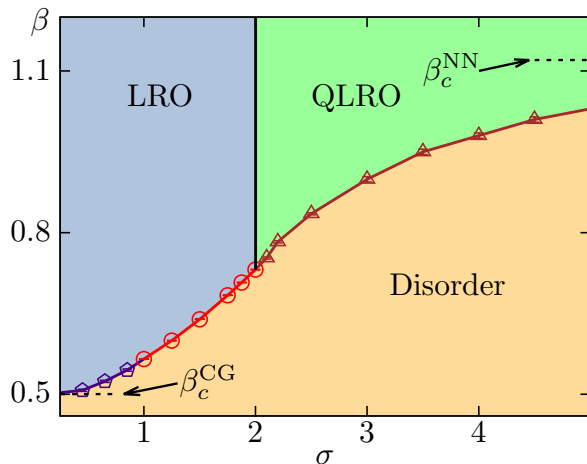


FIG. 1. The phase diagram of the two-dimensional long-range XY model reveals distinct behaviors depending on the interaction range  $\sigma$  and the inverse temperature  $\beta = 1/T$ . In the short-range regime ( $\sigma > 2$ ), the system exhibits BKT transitions (brown line) into a QLRO phase. In the non-classical regime ( $1 < \sigma \leq 2$ ), the system undergoes a continuous phase transition (red line) into a long-range ordered (LRO) phase. Lastly, in the classical regime ( $\sigma \leq 1$ ), the transition (purple lines) is governed by Gaussian theory. The symbols  $\beta_c^{CG}$  and  $\beta_c^{NN}$  denote the critical inverse temperatures for the complete-graph and NN interaction limits, respectively.

regime ( $1 < \sigma \leq 2$ ), and the *short-range* regime ( $\sigma > 2$ ), as illustrated in Fig.1. For  $\sigma < 1$ , the system undergoes a second-order transition to a LRO low- $T$  phase, with critical behavior described by Gaussian mean-field theory [46]. In the short-range regime with  $\sigma > 2$ , the system exhibits a standard BKT transition to a QLRO phase. The non-classical regime ( $1 < \sigma \leq 2$ ) is particularly noteworthy, where detailed FSS analysis reveals a second-order phase transition to a ferromagnetic phase at low- $T$  with  $\sigma$ -dependent critical exponents depending. The phase diagram obtained in this work is inconsistent with the previously suggested one from field theoretical analysis — the proposed intermediate QLRO phase in the regime  $1.75 < \sigma \leq 2$  is not observed from our data [17, 18]. Moreover, our results suggest the crossover point between SR and LR universality is at  $\sigma = 2$ , instead of the  $\sigma = 1.75$  given by Sak’s criterion.

The second-order phase transition in the non-classical regime is evident from the correlation length ratio  $\xi/L$  as a function of inverse temperature  $\beta$  for various  $\sigma$ . Figure 2 presents  $\xi/L$  versus  $\beta$  for  $\sigma = 1.25, 1.75, 1.875, 2, 2.1$  and  $3$ . The data from system sizes ranging from  $L = 64$  to  $L = 4096$  are shown for a comprehensive examination of finite-size effects. For  $\sigma \leq 2$ ,  $\xi/L$  curves of different  $L$ s clearly exhibit a universal intersection at some finite temperature, below which  $\xi/L$  diverges as the system size increases. This typical scaling behavior indicates a second-order phase transition into an LRO phase, and the crossing points mark the location of the critical points  $T_c$ . This differs from the BKT transition

in the SR regime, for which the results are also shown as a comparison. For  $\sigma = 3$ , the  $\xi/L$  curves do not show a crossing; instead, curves for system sizes greater than  $L = 64$  converge to a universal function at low- $T$ , confirming a BKT transition to a QLRO phase. However, at  $\sigma = 2.1$ , a more nuanced behavior occurs. While the  $\xi/L$  curves of smaller system sizes (up to  $L = 1024$ ) seemly suggest a crossing, while those for larger sizes ( $L = 2048$  and  $L = 4096$ ) deviate from this trend and overlap after the critical point. Such behavior reflected the strong finite-size effect near the boundary between LR and SR universality. Nevertheless, as demonstrated in later sections, the low- $T$  and high- $T$  properties of the model further confirm that the system undergoes a BKT transition for  $\sigma = 2.1$ .

#### IV. RESULTS I: LONG-RANGE ORDER AND GOLDSTONE MODE AT LOW TEMPERATURE

In this section, we conduct a comprehensive study of the system’s low-temperature properties. First, in Sec. IV A, we establish the existence of LRO in the low- $T$  phase for  $\sigma \leq 2$ . Following this, in Sec. IV B, we explore the Goldstone mode excitations in the low- $T$  phase for  $\sigma < 2$ , demonstrating that the correlation function adheres to the form  $g(r) = g_0 + cr^{-\eta_\ell}$  where  $\eta_\ell = 2 - \sigma$ . For  $\sigma = 2$ , we propose a possible logarithmic behavior and substantiate it numerically. Subsequently, the QLRO phase at low- $T$ s for  $\sigma > 2$  is discussed in Sec IV C. Finally, we revisit the boundary case of  $\sigma = 2$  and examine its distinctive finite-size scaling in Sec. IV D. Our research primarily focuses on  $\sigma$  values of  $1.75, 1.875, 2$  at various low temperatures characterized by  $\beta = 1, 2, 4, 8$ . Additionally, cases of  $\sigma = 2.1, 3$  are partially included for comparison.

##### A. Long-Range Order for $\sigma \leq 2$

In this part, we demonstrate the existence of LRO in the low- $T$  phase for  $\sigma \leq 2$ . We first study the scaling behavior of the squared correlation length ratio  $(\xi/L)^2$ , which exhibits distinct behavior in the LRO and QLRO phases. Specifically, for given  $T < T_c$ , as the system size increases, this ratio diverges in the LRO phase, while in a QLRO phase, it converges to some non-zero constant. Fig. 3 displays  $(\xi/L)^2$  as a function of  $L$  at inverse temperatures  $\beta = 1$  and  $\beta = 2$  in a semi-logarithmic scale, revealing the distinct low- $T$  scaling behaviors of  $(\xi/L)^2$  for various values of  $\sigma$ . For  $\sigma < 2$ , the curves bend upwards as  $L$  increases, and this divergence can be well-fitted by a power-law function, which will be discussed later. For  $\sigma = 2$ , the data points fall onto a straight line, suggesting that  $(\xi/L)^2$  diverges logarithmically with  $L$ . For both cases, despite the different forms of scaling,  $(\xi/L)^2$  diverges as  $L$  increases, indicating the presence of LRO in the low- $T$  phase for  $\sigma \leq 2$ . In contrast, for  $\sigma > 2$ , the

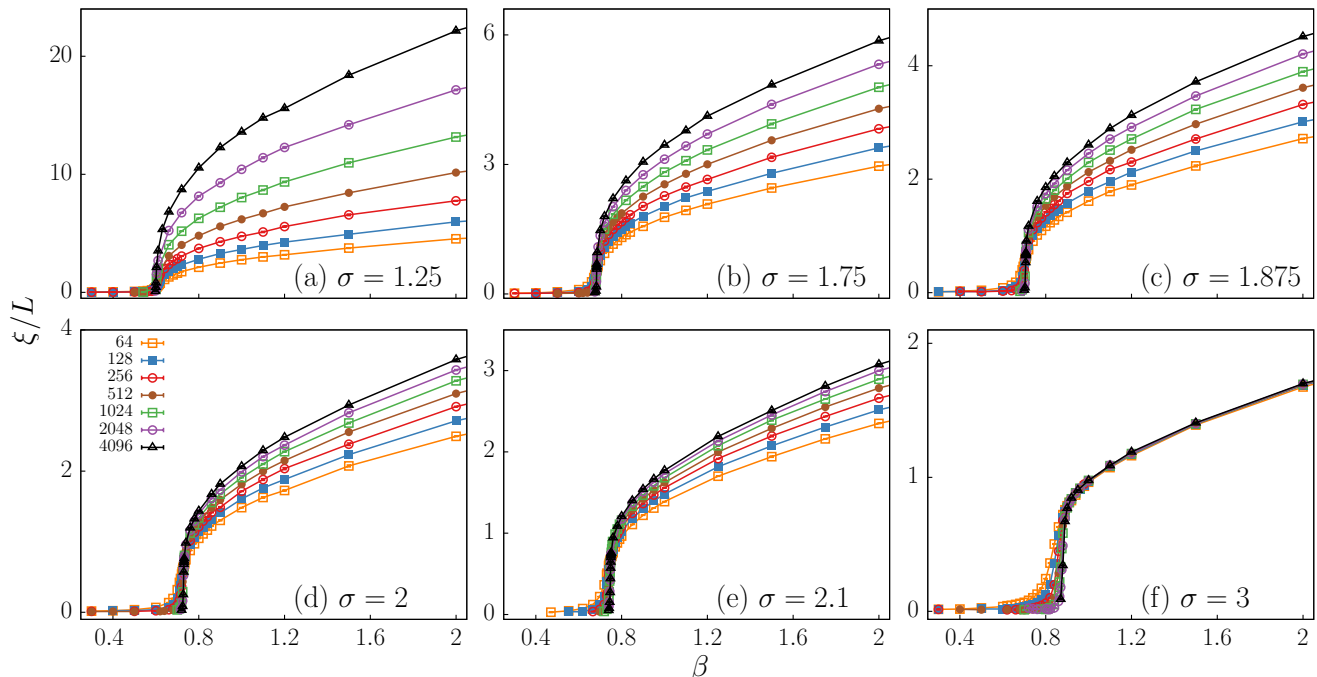


FIG. 2. Overview of the dimensionless ratio  $\xi/L$  for different  $\sigma$  values ( $\xi$  refers to the 2<sup>nd</sup>-moment correlation length). The phase transition type changes from a second-order transition to a BKT-type transition for  $\sigma > 2$ , as shown here. The 2<sup>nd</sup>-moment correlation length divided by  $L$ ,  $\xi/L$ , is plotted as a function of inverse temperature  $\beta$  for various  $\sigma$  values: (a)  $\sigma = 1.25$ , (b)  $\sigma = 1.75$ , (c)  $\sigma = 1.875$ , (d)  $\sigma = 2$ , (e)  $\sigma = 2.1$ , and (f)  $\sigma = 3$ . System sizes range from  $L = 64$  to  $L = 4096$ . For  $\sigma < 2$ , the curves for different system sizes intersect, indicating a second-order phase transition. In the  $\sigma = 2.1$  case, smaller system sizes (up to  $L = 1024$ ) show a crossing due to the strong finite-size effect. However, for larger system sizes ( $L = 2048$  and  $L = 4096$ ), the  $\xi/L$  values tend to overlap beyond the transition point, consistent with a BKT transition. For  $\sigma = 3$ , all curves for  $L > 64$  overlap after the transition point, confirming the BKT transition.

system is in the QLRO phase at low temperatures, and  $(\xi/L)^2$  are expected to converge. This can be seen clearly in the case of  $\sigma = 3$  at both  $\beta = 1$  and 2 where  $(\xi/L)^2$  rapidly converges to a constant as  $L$  increases. However, for  $\sigma = 2.1$  and 2.2, the proximity to the marginal case  $\sigma = 2$  results in strong finite-size effects, leading to a slow convergence of  $(\xi/L)^2$ . As shown in Fig 3, for both  $\beta = 1$  and 2,  $(\xi/L)^2$  curves slowly increase at a slackening rate, and we expect them to finally converge to a constant. In Sec. IV C, we further verify this expectation.

The finite-size scaling of  $\langle M^2 \rangle$  provides another evidence of the LRO in the low- $T$  phase. In the LRO phase,  $\langle M^2 \rangle$  converges to a positive value in the thermodynamic limit, while in the QLRO phase, it reduces to 0 as the system size increases. To extrapolate the value of  $\langle M^2 \rangle$  in the thermodynamic limit, we fit the data at finite system sizes. For the LR XY model, due to the spontaneous breaking of continuous symmetry, the LRO phase shall exhibit Goldstone modes. It is shown in Sec IV B that the correlation function has the form:  $g(x) = g_0 + c \cdot x^{-\eta_\ell}$  where  $\eta_\ell = 2 - \sigma$ . Therefore, considering the relationship between  $\langle M^2 \rangle$  and correlation function:  $\langle M^2 \rangle \sim \frac{1}{L^2} \int g(r) d^2 r$ , we fit the  $\langle M^2 \rangle$  with

following ansatz,

$$\langle M^2 \rangle = g_0 + L^{-\eta_\ell} (a_0 + a_1 L^{-\omega}), \quad (19)$$

where  $a_1 L^{-\omega}$  term accounts for additional corrections. For  $\sigma = 2$ , however, the correlation function can't be easily obtained from a Goldstone mode analysis due to the degeneracy between the LR and the SR interaction terms; nevertheless, in Sec. IV B, we propose a possible scaling form at  $\sigma = 2$ :  $\chi_k \sim L^2 \ln(L/L_0)$  or  $\langle M_k^2 \rangle \sim \ln(L/L_0)$ . Taking into account that  $M_k$  is the Fourier mode of  $M$ ,  $\langle M^2 \rangle$  is likely to exhibit scaling behaviors similar to  $\langle M_k^2 \rangle$ , while its constant term remains preserved. Thus for  $\sigma = 2$ ,  $\langle M^2 \rangle$  should behave as

$$\langle M^2 \rangle = g_0 + \frac{a_0}{\ln(L/L_0)}. \quad (20)$$

A detailed discussion of such logarithmic behavior in the marginal case of  $\sigma = 2$  is provided in the next subsection IV B.

First three panels of Fig. 4 display the extrapolation of  $M^2$  to the  $L \rightarrow \infty$  limit, at various temperatures for  $\sigma = 1.75$  (panel a1),  $\sigma = 1.875$  (panel b1), and  $\sigma = 2$  (panel c1). According to Eq. (19), the leading correction term of  $\langle M^2 \rangle$  is  $L^{-\eta_\ell}$ , thus in panel (a1) and (b1)

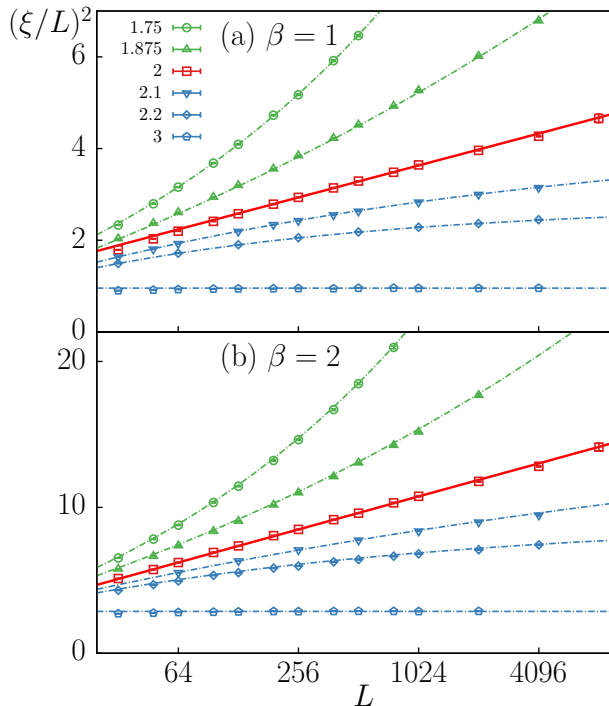


FIG. 3. Different behaviors of  $(\xi/L)^2$  for various  $\sigma$ .  $(\xi/L)^2$  is plotted in the semi-logarithmic coordinates as a function of system size  $L$  is shown for various  $\sigma$  values:  $\sigma = 1.75$  (green circle),  $1.875$  (green upward triangle),  $2$  (red square),  $2.1$  (blue downward triangle),  $2.2$  (blue diamond), and  $3$  (blue pentagon), at inverse temperatures  $\beta = 1$  (a) and  $\beta = 2$  (b). A power-law and logarithmic dependence of  $(\xi/L)^2$  on  $L$  is observed for  $\sigma < 2$  and  $\sigma = 2$ , indicating a divergence as the system size increases, which reflects LRO in the system, whereas, for  $\sigma > 2$ ,  $(\xi/L)^2$  converges to a constant, indicating QLRO in the system.

( $\sigma = 1.75$  and  $1.875$ ), we plot the  $x$ -axis as  $L^{-\eta\epsilon}$ . The plots reveal an asymptotic linear relationship, except for data of small system size, which deviates due to finite-size effects. The non-zero intercepts in the  $y$ -axis reveal the presence of spontaneous magnetization in the low- $T$  phases. Panel (c1) illustrates the logarithmic scaling  $\langle M^2 \rangle$  for  $\sigma = 2$ , where we plot  $\langle M^2 \rangle$  versus  $1/\ln(L/L_0)$ , where  $L_0$  is a fitting parameter. The data fit well to the ansatz in Eq. (20), and spontaneous magnetization is evident from the non-zero intercept. Moreover, the linear relationship observed in this panel confirms the logarithmic scaling of  $M^2$  as described by Eq. (20).

Extrapolating  $\langle M^2 \rangle$  to the thermodynamic limit in the first three panels in Fig. 4 demonstrates the existence of LRO in the low- $T$  phase for  $\sigma \leq 2$ . However, despite the large simulated system size, the slowly decaying corrections result in notable discrepancies between the data and the extrapolated results, particularly in the case of  $\sigma = 2$ . To mitigate these finite-size corrections, we define

the residual magnetization,

$$M_r^2 = \langle M^2 \rangle - b \cdot \langle M_k^2 \rangle, \quad (21)$$

where  $b > 0$  is some constant to be determined. Here,  $\langle M_k^2 \rangle$  is the squared Fourier mode of magnetization, which is closely related to the Fourier transform of the correlation function,  $\langle M_k^2 \rangle \sim \frac{1}{L^2} \int g(r) e^{ikr} d^2r$ . Therefore, for  $\sigma < 2$ ,  $\langle M_k^2 \rangle$  scales as

$$\langle M_k^2 \rangle = L^{-\eta\epsilon} (a_0 + a_1 L^{-\omega}), \quad (22)$$

where  $a_1 L^{-\omega}$  attributes to correction terms. A notable difference between the scaling behavior between  $\langle M^2 \rangle$  and  $\langle M_k^2 \rangle$  is that  $\langle M_k^2 \rangle$  vanishes in the thermodynamic limit. Similarly for  $\sigma = 2$ , we expect  $\langle M_k^2 \rangle$  behaves as,

$$\langle M_k^2 \rangle = \frac{a_0}{\ln(L/L_0)}, \quad (23)$$

again, a detailed discussion on this scaling behavior is provided in the next subsection IV B. Since  $\langle M_k^2 \rangle$  shares the same scaling as the leading correction term in  $\langle M^2 \rangle$ , selecting an appropriate value for  $b$  can effectively cancel out the leading correction, thus reducing the finite-size effects in  $M_r^2$ . More importantly, because  $\langle M_k^2 \rangle$  dwindles and finally vanishes in the thermodynamic limit, for finite system size,  $M_r^2$  is a lower bound of  $\langle M^2 \rangle$ , and in the  $L \rightarrow \infty$  limit, one has  $M_r^2 = \langle M^2 \rangle$ .

In practice, the fitting of equations, such as Eq. (19) and Eq. (23), provides the value of  $a_0$ , which represents the amplitude of the correction term we aim to eliminate. The ratio of  $a_0$  in  $\langle M^2 \rangle$  and  $\langle M_k^2 \rangle$  yields the value of  $b$ . It is important to note that  $b$  remains almost constant for various low temperatures, ensuring this method is broadly applicable in the low- $T$  phase. The residual magnetization  $M_r^2$  is then fitted with the ansatz,

$$M_r^2 = g_0 + a_1 L^{-\omega}, \quad (24)$$

where  $g_0$  is the squared magnetization in the thermodynamic limit, and  $\omega$  is the subleading correction exponent, which remains relatively constant across different temperatures.

The lower three panels of Fig. 4 display  $M_r^2$  as a function of  $L^{-\omega}$  for  $\sigma = 1.75, 1.875, 2$ , with the values of  $b$  and  $\omega$  provided in the figure caption. Thanks to the reduced finite-size corrections, the data points are closer to the extrapolated thermodynamic limit than previous results, and the extrapolated curve clearly intersects the  $y$ -axis at positive values, indicating finite magnetization density. The discrepancies at smaller  $L$  values indicate the presence of additional, smaller corrections beyond  $L^{-\omega}$ . Furthermore, unlike  $\langle M^2 \rangle$ , the coefficient of the leading correction term of  $M_r^2$  is negative, causing  $M_r^2$  to increase with the size of the system. In all cases, the values of  $M_r^2$  for the largest system size are already positive. Consequently, in the  $L \rightarrow \infty$  limit, one must have  $M^2 \geq M_r^2 > 0$ . Thus, we conclude that the system retains long-range order in the low- $T$  phase for  $\sigma \leq 2$ .

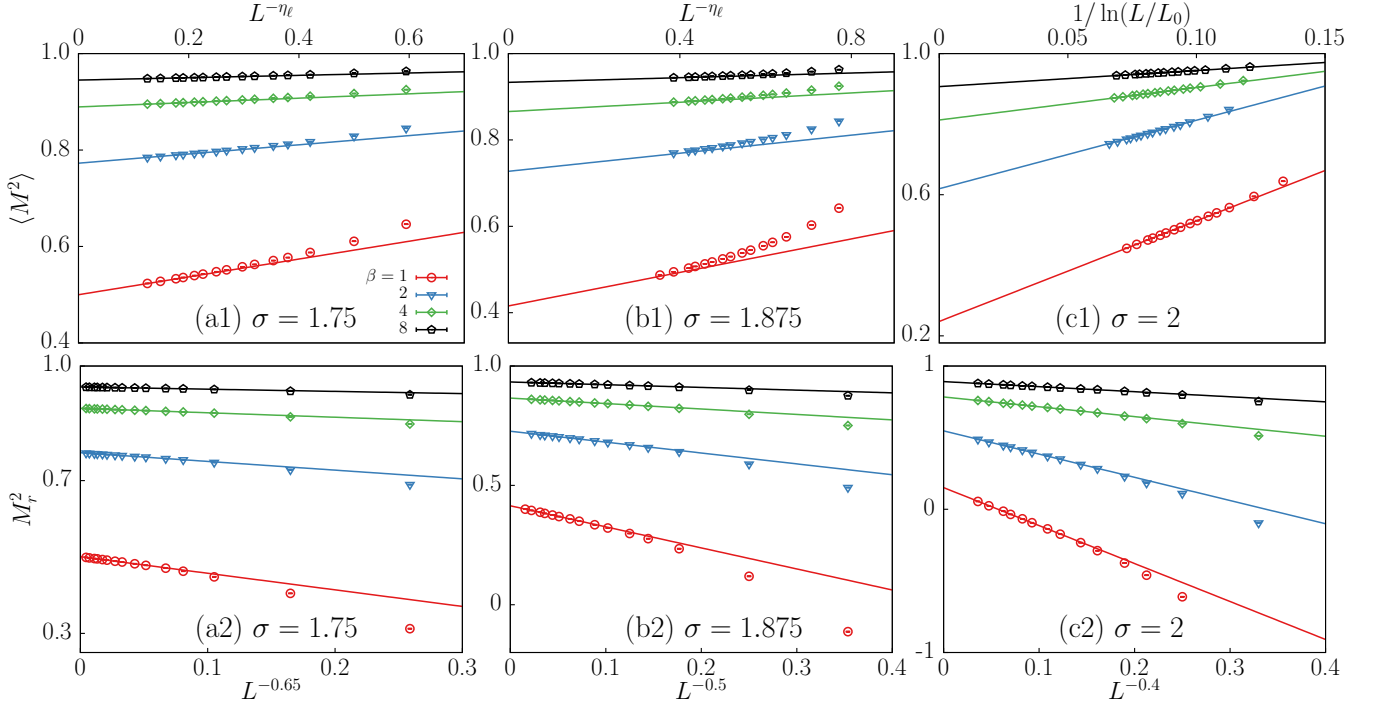


FIG. 4. The existence of spontaneous magnetization for  $\sigma \leq 2$  in low- $T$  phase. The plots of  $\langle M^2 \rangle$  as a function of system size  $L$  for various inverse temperatures  $\beta = 1$  (red), 2 (blue), 4 (green), and 8 (black), at  $\sigma = 1.75$  (a1),  $\sigma = 1.875$  (b1), and  $\sigma = 2$  (c1). The  $x$ -axis representations vary by panel:  $L^{-\eta_\ell}$  ( $\eta_\ell = 0.25, 0.125$  for  $\sigma = 1.75, 1.875$ , respectively) in panels (a1) and (b1),  $1/\ln(L/L_0)$  in panel (c1). The fitting parameter  $L_0$  equals  $e^{-5.4}, e^{-6.8}, e^{-6.38}, e^{-6.2}$  for  $\beta = 1, 2, 4, 8$  in panel (c1). As  $L$  increases, the system approaches the thermodynamic limit, indicating spontaneous magnetization at low temperatures. The figure also includes corresponding plots for  $M_r^2$  in (a2) through (c2) where  $M_r^2$  are defined as  $M_r^2 = \langle M^2 \rangle - b\langle M_k^2 \rangle$ . The  $x$ -axis representations vary by panel:  $L^{-0.65}$  in panel (a2),  $L^{-0.5}$  in panel (b2), and  $L^{-0.4}$  in panel (c2).  $b$  equals 22 for panel (a2), 48 for panel (b2), 149, 175, 152, 154 in  $\beta = 1, 2, 4, 8$  respectively for panel (c2). After subtracting a positive quantity,  $M_r^2$  continues to reach a positive value at the thermodynamic limit with smaller finite-size corrections, which is strong evidence of spontaneous magnetization.

## B. Goldstone Mode

As mentioned in the previous subsection, due to continuous symmetry breaking, we expect Goldstone mode in the LRO phase [47]. In this subsection, we demonstrate, both theoretically and numerically, the algebraic correlation function in the low-temperature phase for  $\sigma < 2$ , i.e.,  $g(x) = g_0 + c \cdot x^{-\eta_\ell}$  with  $\eta_\ell = 2 - \sigma$  ( $x$  and  $g(x)$  represent the distance and correlation between two sites), induced by the Goldstone mode excitation. Moreover, we further speculate and investigate the possible logarithmic behavior of the system at  $\sigma = 2$ .

*Theoretical derivation.* The reduced Hamiltonian of long-range  $O(\mathcal{N})$  model can be written in momentum-

space as [2]:

$$\beta H = \int \frac{d^d q}{(2\pi)^d} \left( \frac{t}{2} + \frac{K_2}{2} q^2 + K_\sigma q^\sigma \right) \Psi(\mathbf{q}) \cdot \Psi(-\mathbf{q}) + \int \frac{d^d q_1}{(2\pi)^d} \int \frac{d^d q_2}{(2\pi)^d} \int \frac{d^d q_3}{(2\pi)^d} u \Psi(\mathbf{q}_1) \cdot \Psi(\mathbf{q}_2) \cdot \Psi(\mathbf{q}_3) \cdot \Psi(-\mathbf{q}_1 - \mathbf{q}_2 - \mathbf{q}_3) \quad (25)$$

where  $\mathbf{q}$  denotes a  $d$ -dimensional momentum variable and  $\Psi(\mathbf{q})$  is the Fourier transform of a locally defined  $n$ -component spin field  $\Psi(\mathbf{x})$  ( $\Psi(\mathbf{x})$  and  $\Psi(\mathbf{q})$  respectively represent the spin field in real space and momentum space. For simplicity, they share the same symbol, and we hope this won't lead to any ambiguities.);  $t, K_2, K_\sigma$ , and  $u$  are interacting parameters, and  $t$  varies linearly with the distance to criticality.

In the last subsection, we have demonstrated the existence of spontaneous magnetization and continuous symmetry breaking at low temperatures for  $\sigma \leq 2$ . Thus, we can adapt mean-field approximation and consider small

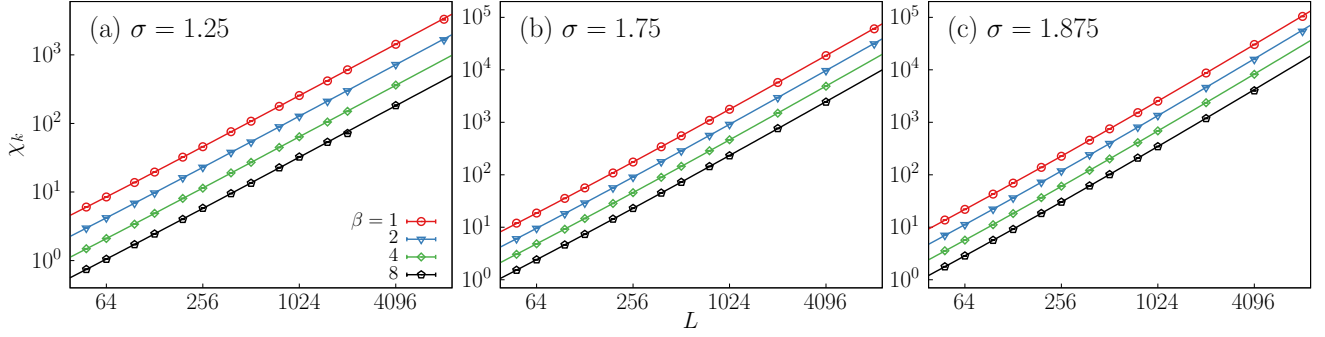


FIG. 5. The log-log plot of  $\chi_k$  versus system size  $L$  for different inverse temperatures  $\beta = 1$  (red), 2 (blue), 4 (green), and 8 (black) at  $\sigma = 1.25$  (a), 1.75 (b), and 1.875 (c) is shown. As  $L$  increases, the data points approach power-law growth with increasing system size  $L$ , confirming the form of correlation function Eq. (32), indicating the presence of a Goldstone mode. Furthermore, the fitting lines at different temperatures are parallel for a certain  $\sigma$ , aligning with the prediction that the value of  $\eta_\ell$  remains independent of temperature.

transverse fluctuations around it:

$$\Psi(\mathbf{x}) = \bar{\Psi}\hat{\mathbf{e}}_l + \Psi_T(\mathbf{x})\hat{\mathbf{e}}_t \quad (26)$$

where  $\hat{\mathbf{e}}_l$  represents the longitudinal direction vector along the mean-field spin direction, while  $\hat{\mathbf{e}}_t$  denotes the transverse direction vector;  $\bar{\Psi} = \sqrt{\frac{t}{4u}}$  is the result of the mean-field approximation and  $\Psi_T$  refers to the transverse fluctuation of magnetization in the transverse directions. Up to the second order, the reduced Hamiltonian becomes[47]:

$$\beta H = V\left(\frac{t}{2}\bar{\Psi}^2 + u\bar{\Psi}^4\right) + \frac{1}{V} \sum_{\mathbf{q}} \left(K_\sigma q^\sigma + \frac{K_2}{2}q^2\right) \cdot |\Psi_T(\mathbf{q})|^2 \quad (27)$$

where  $V$  denotes the volume of the system. For  $\sigma < 2$ ,  $K_\sigma q^\sigma$  is the leading term, and hence  $\frac{K_2}{2}q^2$  can be neglected. Thus, the probability of a particular fluctuation configuration has the Gaussian form:

$$P(\{\Psi_T(\mathbf{q})\}) \propto e^{-\beta H} \propto \prod_{\mathbf{q}} \exp\left(\frac{K_\sigma}{V}q^\sigma \cdot |\Psi_T(\mathbf{q})|^2\right). \quad (28)$$

Hence, the two-point correlation function in the momentum space is:

$$\langle \Psi_T(\mathbf{q})\Psi_T(\mathbf{q}') \rangle = \frac{\delta_{\mathbf{q},-\mathbf{q}'}}{2K_\sigma q^\sigma}, \quad (29)$$

and in the real space is:

$$\begin{aligned} \langle \Psi_T(\mathbf{x})\Psi_T(\mathbf{x}') \rangle &= \frac{1}{V^2} \sum_{\mathbf{q},\mathbf{q}'} \langle \Psi_T(\mathbf{q})\Psi_T(\mathbf{q}') \rangle e^{i\mathbf{q}\cdot\mathbf{x}+i\mathbf{q}'\cdot\mathbf{x}'} \\ &= \frac{1}{V} \sum_{\mathbf{q}} \frac{e^{i\mathbf{q}\cdot(\mathbf{x}-\mathbf{x}')}}{2K_\sigma q^\sigma} \\ &= \frac{1}{2K_\sigma} \int \frac{d^d q}{(2\pi)^d} \frac{e^{i\mathbf{q}\cdot(\mathbf{x}-\mathbf{x}')}}{q^\sigma}. \end{aligned} \quad (30)$$

Considering the integration  $\int \frac{d^d q}{(2\pi)^d} \frac{e^{i\mathbf{q}\cdot\mathbf{x}}}{q^\sigma}$ , divide the integral into angular and radial components and we can analyze its scaling to  $x$  without explicitly computing it (Note that our derivation is under the condition of  $\sigma < 2 = d$ ):

$$\begin{aligned} \int \frac{d^d q}{(2\pi)^d} \frac{e^{i\mathbf{q}\cdot\mathbf{x}}}{q^\sigma} &= \int \frac{d\Omega}{(2\pi)^d} \int dq \frac{e^{iqx \cos \theta}}{q^{\sigma-d+1}} \\ &= x^{\sigma-d} \int \frac{d\Omega}{(2\pi)^d} \int dy \frac{e^{iy \cos \theta}}{y^{\sigma-d+1}} \\ &\sim x^{\sigma-d}. \end{aligned} \quad (31)$$

The correlation function:

$$\begin{aligned} g(x) &= \langle \Psi(\mathbf{x}) \cdot \Psi(0) \rangle \\ &= \bar{\Psi}^2 + \langle \Psi_T(\mathbf{x}) \cdot \Psi_T(0) \rangle \\ &= \bar{\Psi}^2 + c \cdot x^{\sigma-d}. \end{aligned} \quad (32)$$

Hence, for  $\sigma < 2$  at low temperatures, the correlation function takes on an algebraic form:  $g(x) = g_0 + c \cdot x^{-\eta_\ell}$ , with  $\eta_\ell = 2 - \sigma$ . Note that the above derivation is applicable only at low temperatures; thus, we do not need to consider the renormalization of  $K_2 q^2$  terms as the system is far from criticality. Near or at the critical temperature, the system exhibits little to no spontaneous magnetization, and fluctuations play a significant role that cannot be considered negligible anymore. For  $\sigma = 2$ , however, the derivation above is not applicable, and the exact form of the correlation function remains unknown. In Eq. (25), two terms— $\frac{K_2}{2}q^2$  and  $K_\sigma q^\sigma$ —become degenerate, potentially leading to logarithmic behaviors. Next, we present the numerical result to verify the form of the correlation function— $g(x) = g_0 + c \cdot x^{-\eta_\ell}$ —for  $\sigma < 2$ , and the logarithmic behavior of the system at  $\sigma = 2$ .

*Numerical Observation.* We have established that, at low temperatures for  $\sigma < 2$ , the correlation function takes the form:  $g(x) = g_0 + c \cdot x^{-\eta_\ell}$ . While we aim to observe this behavior in our numerical results, directly analyzing the correlation functions poses challenges due

to large finite-size corrections and the unknown constant  $g_0$ . Instead, the Fourier mode of magnetic susceptibility  $\chi_k$  provides a more reliable means of analysis, as the constant term  $g_0$  is effectively canceled out during the Fourier transformation. If the correlation function in Eq. (32) is valid, then  $\chi_k$  should scale according to:  $\chi_k \sim L^{2-\eta_\ell}$ . This scaling relation allows us to verify the system's behavior at low temperatures for  $\sigma < 2$  and confirms whether the predicted power-law decay of correlations holds in our numerical simulations.

Up to the leading finite-size correction term, we propose the fitting ansatz of  $\chi_k$  as,

$$\chi_k = L^{2-\eta_\ell}(a_0 + b_1 L^{-\omega}). \quad (33)$$

With  $\eta_\ell$  fixed at  $2-\sigma$ , the  $\chi_k$  data can be fitted well, and the results are presented in Fig. 5. The figure displays  $\chi_k$  as a function of system size  $L$  in a double-logarithmic plot for  $\sigma = 1.25, 1.75,$  and  $1.875$ . In all cases, the data points for  $\chi_k$  are close to a linear behavior, indicating the anticipated power-law relationship between  $\chi_k$  and  $L$ . The slight upward curvature at smaller system sizes is attributed to finite-size correction terms, which become negligible for sufficiently large  $L$ . This linear trend in the large- $L$  regime demonstrates that the susceptibility follows the scaling relation  $\chi_k \sim L^{2-\eta_\ell}$  and thus confirms the correlation function in Eq. (32). Additionally, the curves for different temperatures are almost parallel across all values of  $\sigma$ , and they can nearly be collapsed onto a single curve through vertical shifting. This observation indicates that the leading scaling exponent  $\eta_\ell$  is temperature-independent. However, when we attempted to relax the value of  $\eta_\ell$  and estimate it through fit using Eq. (33), the results exceeded our expected value of  $2-\sigma$ . This discrepancy is likely due to significant finite-size effects. To mitigate these large finite-size corrections, we further fit  $(\xi/L)^2$  as a function of  $L$  in the low temperature.

At low temperatures, where spontaneous magnetization exists, according to the definition of  $\xi$  in Eq. (10),  $(\xi/L)^2$  is expected to follow the scaling relation:  $(\xi/L)^2 \sim \frac{\langle M^2 \rangle}{\langle M_k^2 \rangle}$ . Since both  $\langle M^2 \rangle$  and  $\langle M_k^2 \rangle$  are subject to similar finite-size corrections, their ratio is likely to cancel out the amplitudes of some communal correction terms, which may lead to a smaller finite-size effect. Considering the scaling form of  $\langle M^2 \rangle$  and  $\langle M_k^2 \rangle$ , i.e. Eq. (19) and Eq. (22),  $(\xi/L)^2$  are fitted to the equation:

$$(\xi/L)^2 = a_0 L^{\eta_\ell} + c. \quad (34)$$

In this approach, without considering any unknown correction terms, the data can be fitted well enough, indicating that  $(\xi/L)^2$  indeed exhibits smaller finite-size correction. The detailed fitting results and final estimates for  $\eta_\ell$  are presented in Table I and Table III, respectively. The results in Table III are consistent with our conjecture that  $\eta_\ell = 2-\sigma$ . While slight deviations are observed for  $\sigma = 1.75$  and  $\sigma = 1.875$  at  $\beta = 1$ , these are reasonable given the proximity to criticality. Our theoretical derivation is most applicable in the low-temperature

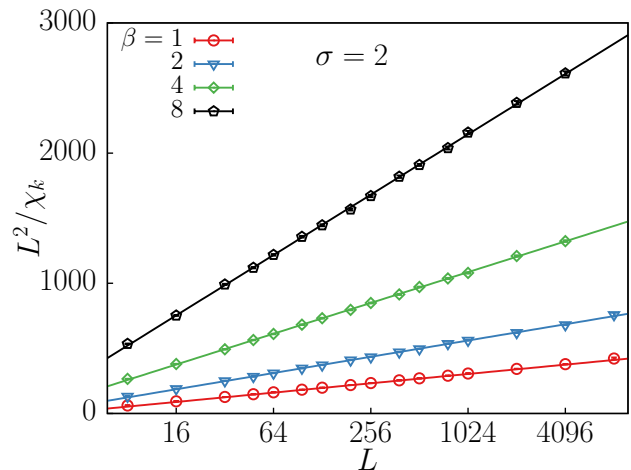


FIG. 6. Demonstration of the logarithmic behavior for  $\sigma = 2$ .  $L^2/\chi_k$  is plotted in the semi-logarithmic coordinate as a function of system size  $L$ , with the  $x$ -axis in logarithmic scale, is shown for different inverse temperatures:  $\beta = 1$  (red),  $\beta = 2$  (blue),  $\beta = 4$  (green), and  $\beta = 8$  (black) at  $\sigma = 2$ . The straight lines indicate the logarithmic behavior:  $\chi_k \sim L^2/\ln(L/L_0)$  for the  $\sigma = 2$  case.

regime, where the system is far from the critical point, and fluctuations are minimal compared to spontaneous magnetization. At even lower temperatures, specifically for  $\beta = 2, 4,$  and  $8$ , all estimated values of  $\eta_\ell$  are compatible with our conjecture."

In the special case of  $\sigma = 2$ , where  $\eta_\ell = 0$ , we speculate that  $\chi_k$  may exhibit a logarithmic scaling behavior, as  $\chi_k \sim L^2 \ln(L/L_0)^{\hat{\eta}_\ell}$ , where  $\hat{\eta}_\ell$  is the critical exponent of the logarithmic correction. To test this hypothesis, we attempt to fit  $\chi_k$  using the following expression:

$$\chi_k = a_0 L^2 (\ln L + c_1)^{\hat{\eta}_\ell}, \quad (35)$$

where  $a_0, L_0,$  and  $\hat{\eta}_\ell$  are unknown parameters. The results of these fits are shown in Table II. It is evident that, across different temperatures, the value of  $\hat{\eta}_\ell$  from the fitting consistently approximates  $-1$ . So we fix  $\hat{\eta}_\ell = -1$  and re-fit  $\chi_k$  to Eq. (35), with results also presented in Table II, supporting a possible scaling behavior:  $\chi_k \sim L^2/\ln(L/L_0)$ .

In Fig. 6, we provide additional evidence by plotting  $L^2/\chi_k$  as a function of  $L$ , with the  $x$ -axis in logarithmic coordinates. All the data points for different low temperatures show linear behavior, indicating  $L^2/\chi_k \sim a \ln L + b$ , which aligns with our assumption that  $\chi_k \sim L^2/\ln(L/L_0)$ .

### C. $\sigma > 2$ cases

It is well-established that for  $\sigma > 2$ , the LR system belongs to the SR universality and exhibits quasi-long-range order (QLRO) at low temperatures. In this subsection, as a comparison to the  $\sigma \leq 2$  case, we briefly demonstrate

TABLE I. Fits of  $(\xi/L)^2$  to Eq. (34) for  $\sigma = 1.25, 1.75$  and  $2$ .

$\sigma$	$\beta$	$L_{\min}$	$\eta_\ell$	$a_0$	$c$	$\chi^2/\text{DF}$	
1.25	1	32	0.751(1)	0.357(4)	-0.46(3)	10.9/11	
		48	0.750(2)	0.361(5)	-0.50(5)	9.8/10	
	2	32	0.755(2)	0.93(1)	-0.9(1)	10.0/10	
		48	0.753(3)	0.95(2)	-1.0(2)	9.1/9	
	4	48	0.750(4)	2.13(6)	-2.6(5)	7.9/9	
		64	0.751(5)	2.10(7)	-2.3(8)	7.6/8	
	8	32	0.746(4)	4.5(1)	-5.2(9)	8.3/9	
		48	0.742(6)	4.6(1)	-6(1)	7.7/8	
	1.75	1	64	0.235(3)	1.98(6)	-2.1(1)	4.6/8
			96	0.235(4)	1.97(9)	-2.1(1)	4.6/7
2		32	0.246(2)	5.2(1)	-5.6(2)	5.5/10	
		48	0.247(3)	5.1(1)	-5.5(2)	5.4/9	
4		32	0.254(2)	10.8(2)	-11.6(4)	3.5/10	
		48	0.253(3)	10.9(3)	-11.7(5)	3.5/9	
8		32	0.250(4)	24(1)	-26(1)	8.1/10	
		48	0.254(5)	23(1)	-24(2)	7.0/9	
1.875		1	32	0.093(3)	6.1(3)	-6.4(4)	7.2/9
			48	0.100(4)	5.5(3)	-5.7(3)	3.9/8
	2	32	0.121(4)	12.0(7)	-12.4(8)	6.5/9	
		48	0.117(6)	13(1)	-13(1)	5.9/8	
	4	32	0.123(7)	27(2)	-28(3)	10.4/9	
		48	0.12(1)	29(4)	-30(4)	9.4/8	
	8	32	0.118(5)	60(4)	-63(5)	4.6/9	
		48	0.126(6)	53(4)	-56(5)	3.2/8	

TABLE II. Fits of  $\chi_k$  to Eq. (35) for  $\sigma = 2$ 

$\beta$	$L_{\min}$	$\hat{\eta}_\ell$	$c_1$	$a_0$	$\chi^2/\text{DF}$
1.0	32	-1.04(1)	-0.86(6)	0.0213(8)	6.6/9
	48	-1.06(2)	-0.8(1)	0.023(1)	5.4/8
	96	-1	-1.06(1)	0.01918(7)	4.0/7
	128	-1	-1.06(2)	0.01919(9)	4.0/6
2.0	48	-0.99(2)	-0.8(1)	0.0108(7)	3.5/8
	64	-0.98(3)	-0.8(1)	0.011(1)	3.5/7
	64	-1	-0.72(1)	0.01107(4)	3.6/8
	96	-1	-0.71(2)	0.01109(5)	3.5/7
4.0	32	-1.03(2)	-0.5(1)	0.0063(4)	4.9/9
	64	-1.04(6)	-0.4(3)	0.007(1)	4.6/7
	96	-1.13(9)	0.1(5)	0.008(2)	3.5/6
	48	-1	-0.57(2)	0.00587(2)	5.4/9
8.0	64	-1	-0.58(2)	0.00585(3)	4.9/8
	48	-1.10(7)	-0.1(3)	0.0039(7)	6.5/7
	64	-1.2(1)	0.3(5)	0.005(1)	5.5/6
	32	-1	-0.50(2)	0.00300(1)	10.1/9
	48	-1	-0.53(3)	0.00299(2)	8.4/8

TABLE III. Estimates of  $\eta_\ell$  for different parameters are provided. The data in the ‘low- $T$ ’ column combines the data from the previous four temperatures, where data in the ‘ $\beta = 1$ ’ column for  $\sigma = 1.75, 1.875$  are discarded for their obvious deviation from other data, which is caused by their proximity to the critical temperature.

$\sigma$	$\beta = 1$	$\beta = 2$	$\beta = 4$	$\beta = 8$	low-T	theory
1.25	0.751(3)	0.754(4)	0.751(5)	0.743(7)	0.751(2)	0.75
1.75	0.237(6)	0.247(3)	0.253(3)	0.250(4)	0.250(2)	0.25
1.875	0.098(8)	0.121(8)	0.123(7)	0.121(9)	0.122(5)	0.125

the low- $T$  properties of the QLRO phase for  $\sigma > 2$ , using  $\sigma = 3$  and  $\sigma = 2.1$  as examples.

Figure 7 plots  $\langle M^2 \rangle$  with  $L$  for  $\sigma = 3$  at double-log coordinates. The linearity of the data points indicates

the scaling behavior  $\langle M^2 \rangle \sim L^{-\eta}$  and hence the correlation function's form:  $g(r) \sim r^{-\eta}$ . As  $L \rightarrow \infty$ ,  $\langle M^2 \rangle$  reduces to 0, thus no spontaneous magnetization at low temperature. Moreover, the slope of the fitted line for the data of  $\beta = 1$  is greater than that of  $\beta = 2$ . This suggests that the value of  $\eta$  decreases as the temperature approaches 0. All these properties are typical signatures of QLRO. The case of  $\sigma = 2.1$  is not presented in Fig. 7 because it exhibits strong finite-size corrections due to the adjacency to  $\sigma = 2$ . As a result,  $\langle M^2 \rangle$  with  $L$  forms a gradually flattening curve, making it difficult to determine whether the curve finally approaches a straight line as in QLRO or converges to a constant as in LRO.

Although it is difficult to study the power-law relationship between  $\langle M^2 \rangle$  and  $L$  for  $\sigma = 2.1$ , the QLRO nature of  $\sigma = 2.1$  can be revealed by analyzing the behavior of  $(\xi/L)^2$ . In Fig. 3, we have compared different behaviors of  $(\xi/L)^2$  for varying  $\sigma$ . The diverging behavior for  $\sigma \leq 2$  indicates the existence of LRO, whereas the converging behavior shows the nature of QLRO. For  $\sigma = 2.1$ , due to significant finite-size corrections,  $(\xi/L)^2$  converges slowly, causing some ambiguity. To clearly demonstrate the converging behavior of  $(\xi/L)^2$ , we perform a fit on its finite-size data. According to Eq. (10), at low temperatures with  $L$  large enough,  $(\xi/L)^2$  has the scaling:  $(\xi/L)^2 \sim \langle M^2 \rangle / \langle M_k^2 \rangle$ . For  $\sigma > 2$ ,  $\langle M^2 \rangle$  and  $\langle M_k^2 \rangle$  share the same leading scaling exponent  $\langle M^2 \rangle \sim \langle M_k^2 \rangle \sim L^{-\eta}$ , but may have different correction terms. Therefore,  $(\xi/L)^2$  should converge to a constant following a series of power-law decays. Thus  $(\xi/L)^2$  can be fitted to:

$$(\xi/L)^2 = a_0 + a_1 L^{-\omega} \quad (36)$$

where  $\omega$  is an unknown correction exponent and needs to be determined by fitting. The fitting results are shown in Fig. 8 with the largest system size up to  $L = 4096$ . The linearity of the data points suggests that  $(\xi/L)^2$  indeed scales in the form of Eq. (36). The finite extrapolated value indicates that  $(\xi/L)^2$  converges to a finite constant in the thermodynamic limit, and hence the system enters a QLRO phase at low temperatures for  $\sigma = 2.1$ .

#### D. Revisiting the low- $T$ properties of the crossover point $\sigma = 2$

The earlier subsections have identified the LRO for  $\sigma \leq 2$  and the QLRO for  $\sigma > 2$  in the low- $T$  phase. To gain deeper insights into the low- $T$  properties of the system at the marginal point of  $\sigma = 2$  and the transition between LRO phase and QLRO phase, we fix the temperature at  $T = 1.0$ , a value that is below the critical temperature  $T_c(\sigma = 2) = 1.3671(4)$  but still sufficiently above the ground state, and observe the 2<sup>nd</sup>-moment correlation length  $\xi$  as a function of  $\sigma$  near  $\sigma = 2$ . We first study the scaling form of  $\xi$  at  $\sigma = 2$ . Sec. IV B has clearly demonstrated the logarithmic scaling behavior of  $\chi_k$ :  $\chi_k \sim L^2 / \ln(L/L_0)$  at  $\sigma = 2$  in the low- $T$  phase.

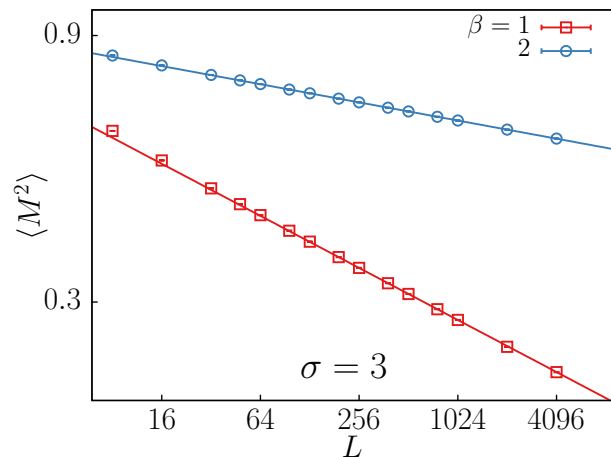


FIG. 7. Demonstration of QLRO in the low- $T$  phase for  $\sigma = 3$ . The square of the magnetization density,  $M^2$ , is plotted against  $L$  using double-logarithmic coordinates. For both  $\beta = 1$  and  $\beta = 2$ , the linearity of the data points indicates a power-law relationship between  $M^2$  and  $L$ , which is the signature of QLRO.

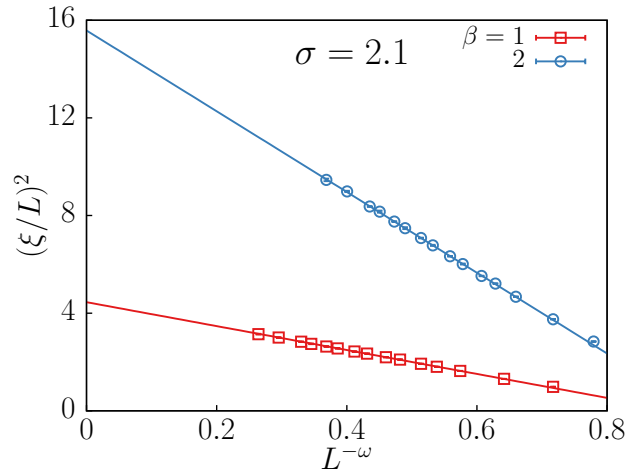


FIG. 8. Fitting results of Eq. (36) for  $\sigma = 2.1$  at  $\beta = 1$  and  $\beta = 2$ . The  $x$ -axis is  $L^{-\omega}$ , with  $\omega = 0.16$  for  $\beta = 1$  and  $0.12$  for  $\beta = 2$ . The good agreement between the fitted line and the scatter points demonstrates the quality of the fit, and the  $y$ -intercept of the line provides the finite value of  $(\xi/L)^2$  in the thermodynamic limit, suggesting the presence of QLRO.

Considering the definition Eq. (10) and the spontaneous magnetization in the low- $T$  phase, the 2<sup>nd</sup>-moment correlation length  $\xi$  should exhibit similar logarithmic scaling form:  $\xi \sim L \sqrt{\frac{\langle M^2 \rangle}{\langle M_k^2 \rangle}} \sim L \ln(L/L_0)^{\frac{1}{2}}$ . Next, by examining the behavior of  $\xi$  as a function of  $\sigma$  near  $\sigma = 2$ , we can explore the transition between different scaling regimes and better understand how the system evolves as  $\sigma$  varies.

Figure 9 presents a detailed finite-size scaling analysis of  $(\xi/L)^2 / \ln(L/L_0)$  as a function of  $\sigma$  for several system sizes  $L$ . Here, the constant  $L_0 = 2.9$  according to the Table II. A key feature of this figure is the clear crossing of

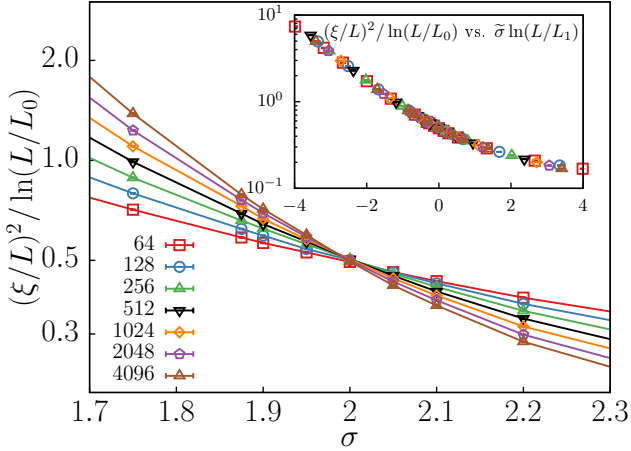


FIG. 9. The semi-logarithmic plot of  $(\xi/L)^2/\ln(L/L_0)$  as a function of  $\sigma$  for several system sizes  $L = 64$  to  $4096$ , with  $y$ -axis in logarithmic scale. The inset shows the data collapse of  $(\xi/L)^2/\ln(L/L_0)$  vs.  $\tilde{\sigma} \ln(L/L_1)$ , where  $\tilde{\sigma} = \sigma - 2$ ,  $L_0 = 2.9$  and  $L_1 = 3.0$ .

curves at  $\sigma = 2$ , marking a shift from LRO to QLRO. To capture the behavior near  $\sigma = 2$ , we conjecture a refined scaling form for the 2<sup>nd</sup>-moment correlation length, taking into account logarithmic corrections at  $\sigma = 2$  in the low-temperature phase  $T < T_c$ . Specifically, we propose that  $\xi$  scales as:

$$\xi = L \ln(L/L_0)^{\frac{1}{2}} \xi'(\tilde{\sigma} \ln(L/L_1)), \quad (37)$$

where  $\tilde{\sigma} = \sigma - 2$  represents the deviation from  $\sigma_*$ ,  $\xi'$  is a universal scaling function that governs the behavior near  $\sigma = 2$ , and  $L_0$  and  $L_1$  are constants yet to be determined through data fitting. This scaling form accounts for the logarithmic corrections to the correlation length at the critical point, providing a more accurate description of the system's behavior as  $\sigma$  approaches 2 from either side. The inset of Fig. 9 demonstrates the efficacy of this scaling hypothesis by showing a collapse of the scaled  $\xi$  data points onto a single, universal curve. This data collapse provides numerical support for the conjectured scaling form and further confirms that  $\sigma = 2$  represents a marginal point where the system undergoes a transition between the LRO and QLRO phases at low temperatures.

## V. RESULTS II: POWER-LAW DIVERGENCE OF CORRELATION LENGTH AT HIGH TEMPERATURE

In this section, we focus on the physical properties of the high- $T$  phase as the system approaches the critical point at  $\beta_c$  from the disordered phase. Specifically, we investigate the growth of the second-moment correlation length  $\xi$  and susceptibility  $\chi$ . The growth form of  $\xi$  and  $\chi$  depends on the type of the transition, providing a clearer

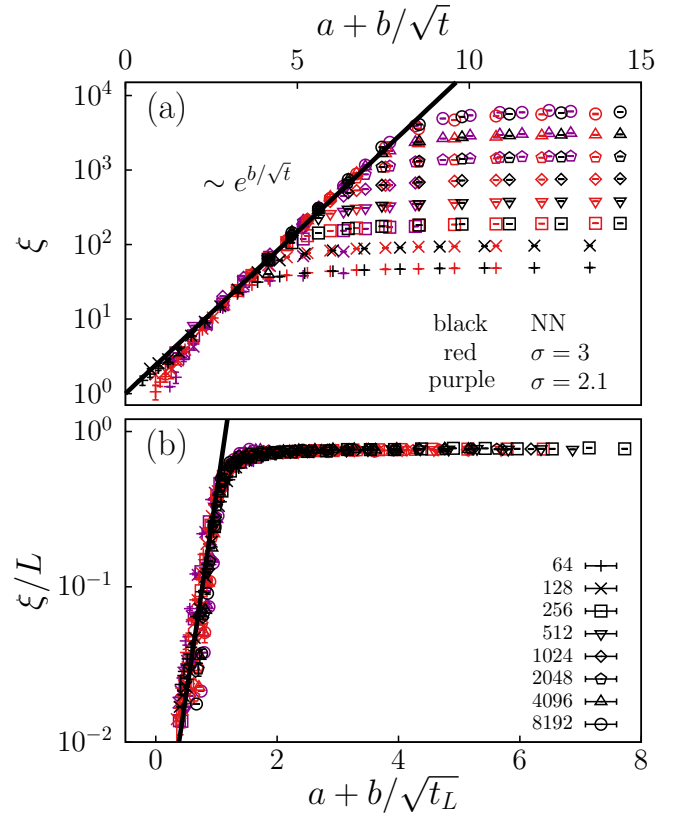


FIG. 10. Demonstration of the exponential growth of  $\xi$  and corresponding FSS, indicating the BKT transition for  $\sigma > 2$ . (a) The semi-logarithmic plot of  $\xi$  as a function of  $a + b/\sqrt{t}$  for  $\sigma = 2.1$  (purple), 3 (red) and NN case (black), where  $t = (T - T_c)/T_c$  and the non-universal constants are  $a = 0.69, -0.22, -1.20$  and  $b = 0.6, 1.1, 1.7$ , respectively. (b) The semi-logarithmic plot of the ratio  $\xi/L$  as a function of  $a + b/\sqrt{t_L}$ , where  $t_L = t[\ln(L/L_0)]^2$  with the non-universal length scale simply set by  $L_0 = 1$ . Here, the non-universal constants are  $a = 0, 0.12, 0.25$  and  $b = 0.6, 1.1, 1.7$ , respectively.

indication of universality than critical exponents and allowing one to identify the threshold between SR and LR universality. The critical points  $\beta_c$  for  $\sigma = 1.875, 2, 2.1$ , and 3 are determined through FSS analysis, whose value can be found in Table IV; for the NN case, previous numerical investigation gives  $\beta_c = 1.11996(6)$  [48].

As the system approaches the critical point of a BKT transition from a disordered phase,  $\xi$  and  $\chi$  diverge exponentially as  $\sim \exp(b/\sqrt{t})$  [49, 50], where  $t = (T - T_c)/T_c$  is the reduced temperature, and  $b$  is a non-universal constant. As shown in Fig. 10(a), a semi-logarithmic plot of  $\xi$  versus  $a + b\sqrt{t}$  is presented for  $\sigma = 2.1$  (purple), 3 (red), and the NN case (black), where the non-universal constant  $a$  comes from the amplitude of the scaling  $\sim \exp(b/\sqrt{t})$ , and the specific values of  $a$  and  $b$  are provided in the corresponding caption.

In the critical scaling regime, for a given  $t$ ,  $\xi$  quickly converges to its thermodynamical value as  $L$  increases.

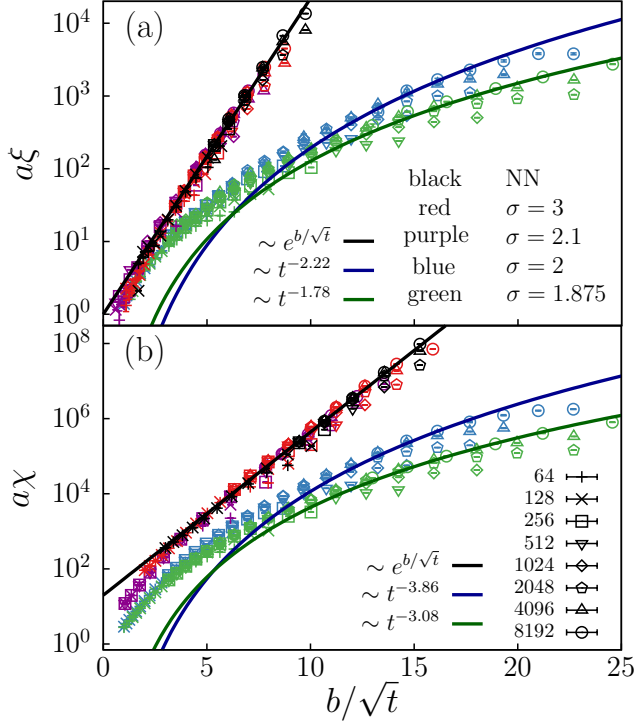


FIG. 11. Deviation of the 2<sup>nd</sup>-moment correlation length  $\xi$  and susceptibility  $\chi$  growth at  $\sigma = 2$  from the BKT scaling. Panel (a) shows a semi-logarithmic plot of  $a\xi$  as a function of  $b/\sqrt{t}$  for various  $L$  at  $\sigma = 1.875$  (green), 2 (blue), 2.1 (purple), 3 (red), and the NN case (black), where the reduced temperature is  $t = (T - T_c)/T_c$ , and  $a = 1, 1, 0.5, 1.25, 3.33$  and  $b = 1, 1, 0.6, 1.1, 1.7$ , respectively. Panel (b) shows a semi-logarithmic plot of  $a\chi$  as a function of  $b/\sqrt{t}$  for various  $L$  at  $\sigma = 1.875$  (green), 2 (blue), 2.1 (purple), 3 (red), and the NN case (black), where  $a = 1, 1, 4, 23.53, 66.67$  and  $b = 1, 1, 1.05, 2, 3$ , respectively. For the  $\sigma = 2.1, 3$ , and NN case, the black solid line, which scales as  $e^{b/\sqrt{t}}$ , serves as a guide to the eye for the exponential growth of  $\xi$  and  $\chi$ , characterizing the BKT transition. However, for  $\sigma = 1.875$  and 2, the dark-green and dark-blue curved lines, scaling as  $t^{-1.78}$  and  $t^{-2.22}$  in panel (a), and  $t^{-3.08}$  and  $t^{-3.86}$  in panel (b), serve as guides to the eye for the power-law growth of  $\xi$  and  $\chi$ , indicating a second-order phase transition.

The growth of  $\xi$  at large  $L$  as a function of  $t$  then reveals the thermodynamic growth law of correlation length; however, when the system enters the finite-size critical window, where  $\xi \sim L$ , the  $\xi$  curve begins to bend to a plateau due to finite-size scaling behavior, thus deviating from the thermodynamic growth law. Note that this analysis is different from the FSS analysis. Here, one first takes the  $L \rightarrow \infty$  limit for a given temperature  $T$  and then takes the  $T \rightarrow T_c$  limit to examine the asymptotic growth law of  $\xi$ . In contrast, the FSS analysis first takes the  $T \rightarrow T_c$  limit for a given  $L$ , followed by the  $L \rightarrow \infty$  limit, studying the scaling behavior within the finite-size critical window. As shown in Fig. 10(a), the straight black line in the semi-log plot clearly demon-

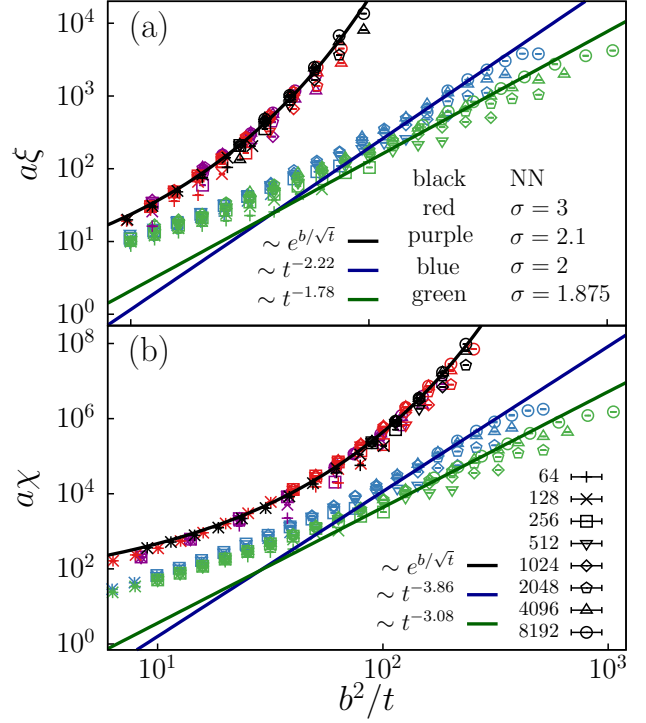


FIG. 12. Growth of the 2<sup>nd</sup>-moment correlation length  $\xi$  and susceptibility  $\chi$  growth at various  $\sigma$  in double-logarithmic scale. Panel (a) shows  $a\xi$  as a function of  $b^2/t$  for various  $L$  at  $\sigma = 1.875$  (green), 2 (blue), 2.1 (purple), 3 (red), and the NN case (black), where the reduced temperature is  $t = (T - T_c)/T_c$ . Panel (b) shows  $a\chi$  as a function of  $b^2/t$  for various  $L$  at  $\sigma = 1.875$  (green), 2 (blue), 2.1 (purple), 3 (red), and the NN case (black). The values of  $a$  and  $b$  are the same as those in Fig. 11. For  $\sigma = 1.875$  and 2,  $\xi$  and  $\chi$  asymptotically follow a power-law growth, indicating a second-order phase transition. As a comparison, for  $\sigma = 2.1, 3$ , and NN cases, the exponential growth of  $\xi$  and  $\chi$  for a BKT transition can be observed (the black curve).

strates the exponential growth of  $\xi$  for  $\sigma > 2$ , the typical BKT scaling behavior. In the large  $t$  regime (the bottom left corner of Fig. 10(a)), where the system is far from criticality,  $\xi$  slightly deviates from the exponential growth. Moreover, in Fig. 10(b), we further plot the ratio  $\xi/L$  versus  $b/\sqrt{tL} = b/\sqrt{t(\ln L/L_0)^2}$  to examine the FSS of the exponential growth, where  $L_0$  is non-universal length scale, simply set as 1. The scaling field  $t_L$  [51, 52] originates from the exponential divergence of the correlation length near the BKT transition  $\xi \sim L \sim \exp(b/\sqrt{t})$ . The data points collapse onto a single curve, showing that for  $\sigma > 2$ , the phase transitions belong to the BKT universality class.

On the other hand, near a second-order transition,  $\xi$  diverges algebraically as  $\xi \sim t^{-\nu}$ , with  $\nu$  as the correlation length exponent, and  $\chi$  diverges algebraically as  $\chi \sim t^{-\gamma}$ , with  $\gamma$  as the susceptibility exponent. Hence, by investigating the growth of  $\xi$  and  $\chi$  near  $\beta_c$ , we can

readily reveal the type of transition at different  $\sigma$ , particularly the transition at  $\sigma = 2$ .

In Fig. 11(a), a semi-logarithmic plot of  $a\xi$  versus  $b/\sqrt{t}$  for various  $\sigma$  is presented. The non-universal constants  $a$  and  $b$ , obtained through the fitting, enhance the overall readability of plots without affecting the universal growth law. The specific values of  $a$  and  $b$  are provided in the corresponding caption. For  $\sigma = 2.1$  (purple),  $\sigma = 3$  (red), and the NN case (black), the straight black line demonstrates that the correlation length diverges exponentially  $\xi \sim \exp(b/\sqrt{t})$ , characterizing a typical BKT transition. For clarity, we exclude certain data points in the finite-size critical window, which manifests as a plateau. For  $\sigma = 1.875$  (green) and 2 (blue), when sufficiently away from  $\beta_c$ , i.e.  $b/\sqrt{t}$  approaches 0,  $\xi$  behaves seemingly like that for  $\sigma = 2.1, 3$  and the NN case. However, near the critical point, i.e., as  $b/\sqrt{t}$  approaches infinity, the behavior of  $\xi$  becomes increasingly different from SR cases ( $\sigma > 2$ ) and deviates from the exponential growth, suggesting a different universality class. In fact, the growth of  $\xi$  for  $\sigma = 1.875$  and 2 can be well-fitted using a power-law function (the curved lines in dark green and dark blue), indicating a second-order transition. In Fig. 11(b), a similar analysis is applied to the susceptibility,  $\chi$ . The plot shows  $a\chi$  versus  $b/\sqrt{t}$  on a semi-logarithmic scale. For the BKT cases ( $\sigma = 2.1, 3$ , and NN),  $\chi$  diverges exponentially, with the straight black line guiding the eye. On the other hand, for  $\sigma = 1.875$  and 2,  $\chi$  follows a power-law growth near the critical point, with the dark-blue and dark-green curved lines guiding the eye, suggesting a second-order phase transition.

Figure. 12 presents the log-log plot of  $a\xi$  and  $a\chi$  versus  $b^2/t$ , where the x-axis is the square of  $b/\sqrt{t}$ . In Fig. 12(a), for  $\sigma = 1.875$  and 2, the growth of  $\xi$  asymptotically follows a linear relation as  $b^2/t \rightarrow \infty$  (the straight dark-green and dark-blue lines), consistent with the power-law growth behavior of a second-order transition. The deviation of  $\xi$  from linearity and the discrepancy between the exponent estimated from Fig. 12(a) and fitting result in Table V are likely due to the strong correction to scaling from the irrelevant fields. Specifically,  $\xi \sim t^{-\nu}g(u/t^{y_u/y_t})$ , where  $u$  is some irrelevant field and  $y_u < 0$  is the corresponding scaling exponent. Nevertheless, the growth behavior of  $\xi$  can clearly reveal the type of phase transition for various  $\sigma$ . Similarly, for the growth of  $\chi$  in Fig. 12(b), the straight dark-green and dark-blue lines illustrate a power-law behavior, as  $\chi \sim t^{-\gamma}$  for  $\sigma = 1.875$  and 2, again indicating a second-order transition. As  $b^2/t$  approaches infinity, the slopes provide the critical exponent  $\gamma$ , and through the hyperscaling relation  $\gamma = \nu(2 - \eta)$ , these values are also consistent with those listed in Table V. In all, our analysis of the growth behavior of  $\xi$  and  $\chi$  strongly suggests that the system undergoes a second-order transition for  $\sigma \leq 2$ , while a BKT transition for  $\sigma > 2$ ; hence, the threshold between SR and LR universality is at  $\sigma_* = 2$ .

## VI. RESULTS III: CRITICAL POINTS AND CRITICAL EXPONENTS

In the previous sections, we have studied the low- $T$  and high- $T$  properties of the system for  $\sigma \leq 2$ . In this section, we focus on the system's critical properties for  $\sigma \leq 2$ . The fitting of the critical point and critical exponent is elaborated in Sec. VIA and VIB, respectively. Then, to determine the reliability of the estimate of  $\eta$ , the correlation function is also studied in Sec. VIC.

### A. The Fitting of Critical Point

In this subsection, we focus on determining the critical temperature for various values of  $\sigma$ . For  $\sigma \leq 2$ , a second-order phase transition from a disordered phase to a ferromagnetic phase is expected, where the dimensionless ratio curves, such as  $Q_m$  and  $\xi/L$ , for different system sizes, should ideally intersect at the critical point. Figure 13 presents  $\xi/L$  as a function of inverse temperature  $\beta$  for system sizes ranging from  $L = 64$  to  $L = 4096$ , and for  $\sigma = 1.75, 1.875$ , and 2.0. Unlike Figure 2, which covers a broader range, this figure zooms in on a small regime of  $\beta$  to observe the crossing behavior of  $\xi/L$  for different system sizes. However, Figure 13 shows that the crossing points for different system sizes do not converge at a single value of  $\beta$ . Instead, these points shift toward higher values of  $\beta$  as the system size increases, a phenomenon attributed to finite-size effects. The distance between the crossing points decreases as the system size grows, indicating that with larger system sizes, the crossing points will eventually converge at a single value of  $\beta$ , marking the critical point. To confirm this behavior and accurately determine the critical point, a finite-size analysis is performed to the crossing point  $\beta_L$  between system sizes of  $L$  and  $L/2$ .

The final crossing point, or critical inverse temperature  $\beta_c$ , is obtained by fitting  $\beta_L$  to the following equation:

$$\beta_L = \beta_c + aL^{-\omega}, \quad (38)$$

where  $\omega$  is related to the correlation length exponent  $\nu$  and the leading irrelevant exponent in the renormalization group framework. Figure 14 illustrates the fitting results, with the  $x$ -axis representing  $L^{-\omega}$  and the  $y$ -axis showing the corresponding values of  $\beta_L$ . In each case, the fitting lines exhibit finite intercepts on the  $y$ -axis, highlighted by red stripes. This confirms that the  $\xi/L$  curves finally intersect at a single critical point as the system size increases. The intercepts provide an estimate of the critical temperature  $\beta_c$ . For further accuracy, the dimensionless ratios, such as  $\xi/L$  and  $Q_m$ , are also fitted with respect to  $L$  and  $\epsilon = 1/T - 1/T_c$  near the critical point to refine the estimate of the critical point.  $\epsilon = \frac{1}{T} - \frac{1}{T_c}$  is used to replace  $t$  for the convenience of fitting:

$$t = a_1(T - T_c) + O((T - T_c)^2) = b_1\epsilon + O(\epsilon^2). \quad (39)$$

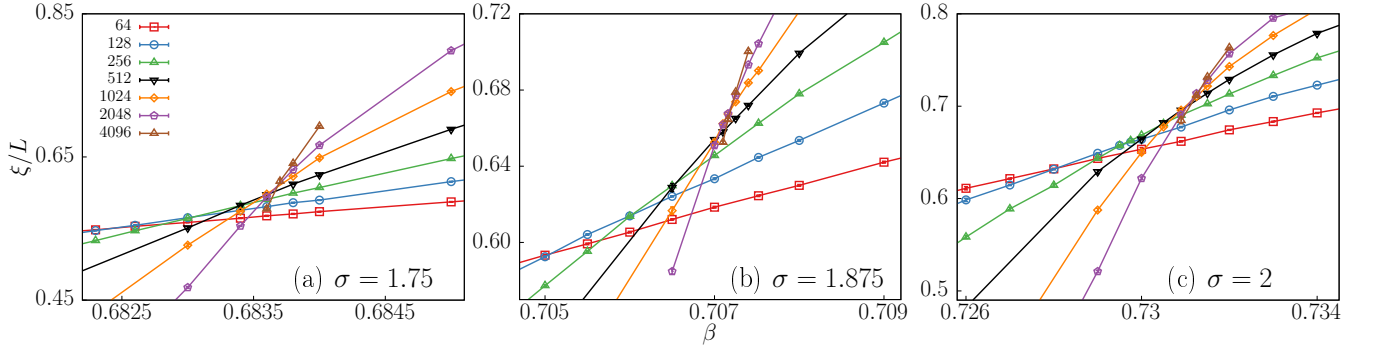


FIG. 13. The zoom-in of the 2nd-moment correlation length divided by  $L$ ,  $\xi/L$ , as a function of inverse temperature  $\beta$  for various system sizes, ranging from  $L = 64$  to  $L = 4096$ , is shown across three different values of  $\sigma$ : 1.75 (a), 1.875 (b), and 2 (c). Clear crossing behavior can be observed in all the cases, despite the shift of crossing point due to the finite-size effect.

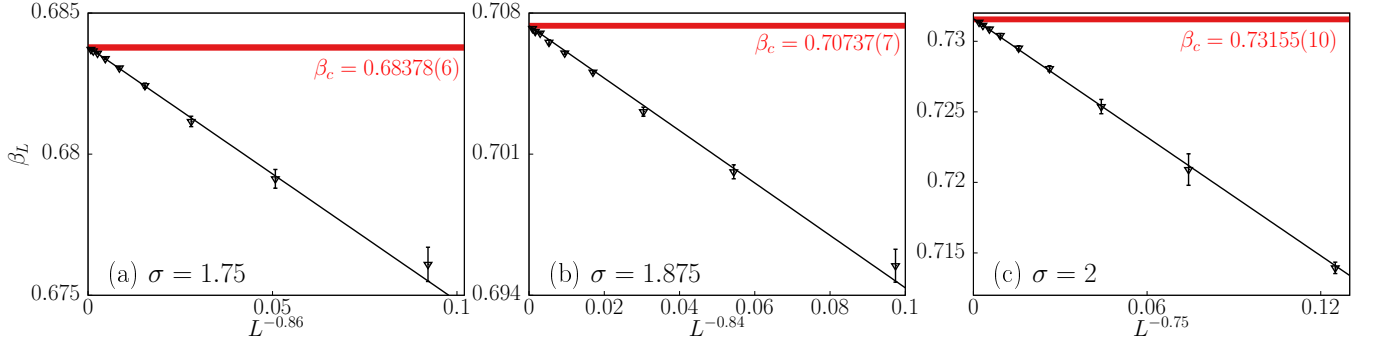


FIG. 14. The extrapolation of  $\xi/L$  curves' crossing point  $\beta_L$  of different system sizes. The  $x$ -axis represents the correction term  $L^{-\omega}$ :  $L^{-0.86}$  in panel (a),  $L^{-0.84}$  in panel (b), and  $L^{-0.75}$  in panel (c), while the  $y$ -axis denotes the inverse temperature  $\beta$  at which the correlation length ratios for two consecutive system sizes intersect. The red line indicates the extrapolated value of  $\beta$  as the system size approaches infinity.

Considering the universal part of dimensionless ratio  $Q$  as in Eq. (17) and (18), Certain Taylor expansion provides a fitting equation of  $Q$ :

$$Q(t, u, L) = a_0 + \sum_{i=1}^m a_i (\epsilon L^{y_t})^i + b_1 L^{-\omega} + b_2 L^{-2\omega} + c_1 \epsilon L^{y_t - \omega} + c_2 \epsilon^2 L^{2y_t - \omega}, \quad (40)$$

where the value of  $m$  depends on the specific fitting process and is typically taken as 2 or 3;  $L^{-\omega}$  term comes from the irrelevant field  $u$ , and  $\omega = -y_u$ . In the formula above, terms such as  $\epsilon^2 L^{y_t}$ ,  $\epsilon^3 L^{y_t}$ ,  $\epsilon^3 L^{2y_t}$ ,  $\dots$ , are not under consideration because according to experiments, including such terms in the specific fitting process has almost no impact on the fit, and their amplitudes are also very close to zero. For the fit of  $Q$ , when  $\sigma \leq 1.5$ ,  $Q_m$  is more suitable for fitting, whereas when  $1.5 < \sigma \leq 2$ ,  $\xi/L$  provides a better fit. By combining the two quantities, relatively accurate estimates of critical points can be obtained, and they are consistent with those derived from the fit of  $\beta_L$ . The final estimated values of  $\beta_c$  are presented in Table IV (Note that, except for  $\sigma = 1.25, 1.5, 1.75, 1.875$  and 2, the critical points under other parameters are only determined with much less precision since they are mainly

used for drawing the phase diagram in Fig. 1).

TABLE IV. Estimations of critical point  $\beta_c$  for various  $\sigma$  shown in Fig. 1.

$\sigma$	$\beta_c$	$\sigma$	$\beta_c$
0.25	0.503(2)	2	0.7315(2)
0.45	0.5075(2)	2.1	0.753(2)
0.65	0.524(2)	2.2	0.783(2)
0.85	0.545(2)	2.5	0.835(2)
1	0.5654(1)	3	0.899(5)
1.25	0.599615(6)	3.5	0.950(5)
1.5	0.63936(1)	4	0.980(5)
1.75	0.68380(7)	4.5	1.010(5)
1.875	0.70737(7)	5	1.030(5)

As a supplement, we briefly introduce the method to determine the critical point for  $\sigma > 2$ . When  $\sigma > 2$ , the system undergoes a BKT transition, where the susceptibility  $\chi$  is known to follow the scaling behavior:  $\chi \sim L^{7/4} (\ln L + C_1)^{1/8}$  at the critical point [53] where  $C_1$  is a nonuniversal constant and needs to be obtained through fitting. Therefore, plotting  $\chi L^{-7/4} (\ln L + C_1)^{-1/8}$  as a function of temperature, the curves of different system sizes intersect at the critical point.

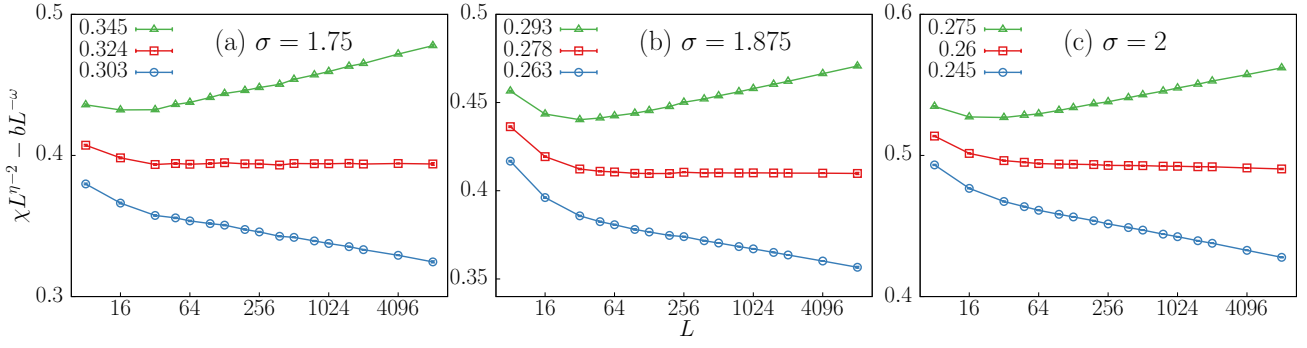


FIG. 15. Demonstration of the reliability of the fitting of  $\chi$ . The semi-logarithmic plots of  $\chi L^{\eta-2} - bL^{-\omega}$  versus  $L$  for  $\sigma = 1.75, 1.875$ , and  $2$  are shown (where  $\omega = 0.48, 0.42, 0.5$  respectively). The red square approaches a horizontal line as  $L \rightarrow \infty$ , indicating the precise estimate for  $\eta$  that we obtain.

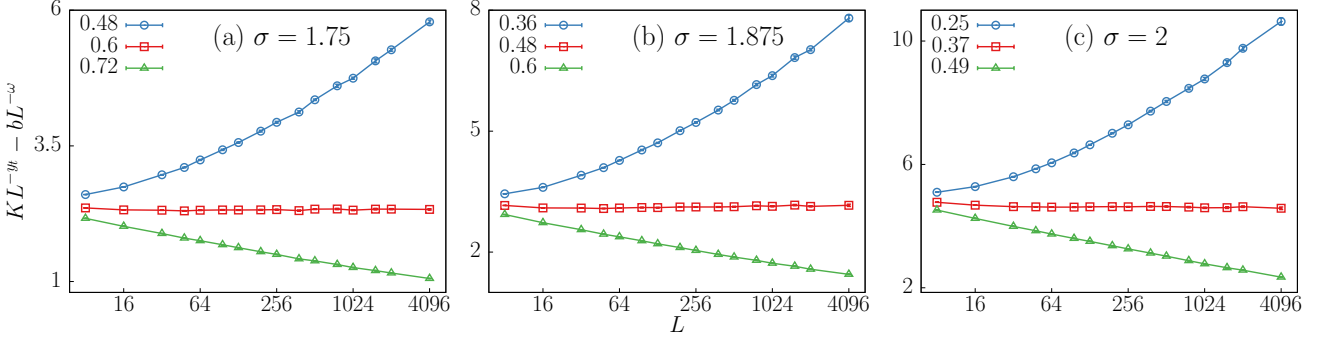


FIG. 16. Demonstration of the reliability of the fitting of  $K$ . The semi-logarithmic plots of  $K L^{-y_t} - bL^{-\omega}$  versus  $L$  for  $\sigma = 1.75, 1.875$ , and  $2$  are shown (where  $\omega = 0.25, 0.25, 0.2$  respectively). The red square approaches a horizontal line as  $L \rightarrow \infty$ , indicating the precise estimate for  $y_t$  that we obtain (note that  $y_t = 1/\nu$ ). It is worth noting that, compared to  $\chi$ , the covariance  $K$  exhibits larger errors at various data points. This is particularly evident for  $L = 8192$ , where the difficulty in simulating longer Markov chain lengths results in significant errors for  $K$  under this parameter. Therefore, the data point for  $L = 8192$  is not included in the fitting of  $K$ .

## B. The Fitting of Critical Exponents

According to the scaling relationship, only two critical exponents are independent, and here we mainly focus on  $\eta$  and the thermal scaling exponent  $y_t$  (note the relationship between  $y_t$  and the critical exponent  $\nu$ :  $\nu = 1/y_t$ ). In Sak's criterion,  $\eta = \max(2 - \sigma, \eta_{\text{SR}})$  where  $\eta_{\text{SR}} = \frac{1}{4}$  for 2D XY model, so estimating the value of  $\eta$  is another way to determine whether  $\sigma_*$  equals 1.75 or 2. By fitting the susceptibility  $\chi$  and the scaled covariance  $K$ , the values of  $\eta$  and  $y_t$  can be numerically estimated. At the critical point, considering the finite-size scaling Eq. (14) and (16),  $\chi$  and  $K$  are respectively fitted to:

$$\chi = L^{2-\eta}(a + b \cdot L^{-\omega}) + c \quad (41)$$

and

$$K = L^{y_t}(a + b \cdot L^{-\omega}) + cL^{\eta-2}, \quad (42)$$

where  $b \cdot L^{-\omega}$  refers to the finite-size correction and  $c$  derives from the analytic part of freedom energy. During the fitting process, various values of  $\omega$  are tested.

It is observed that when  $\omega$  is excessively large or small, the data cannot be adequately fitted. However, when  $\omega$  falls within a certain range, an appropriate fit yields reliable estimates for exponents. The details and results of the fitting are shown in Tables VI, VII and V, respectively. Figure 15 and 16 visually show the reliability of the fitting. To be specific, when taking the estimated value of  $\eta$  and  $y_t$ , according to the fitting,  $\chi L^{\eta-2} - bL^{-\omega}$  and  $K L^{-y_t} - bL^{-\omega}$  should converge to a non-zero value as  $L$  increases; otherwise they'll either diverge or reduce to 0. It can be seen that in both figures, curves cor-

TABLE V. Estimates of two exponents  $y_t$  and  $\eta$  for non-classical regime. The results are obtained from the fitting: Eq. (41) and (42).

$\sigma$	$y_t$	$\eta$
1.25	0.987(4)	0.75(1)
1.5	0.86(3)	0.518(8)
1.75	0.60(4)	0.324(7)
1.875	0.48(4)	0.278(5)
2	0.37(4)	0.260(5)

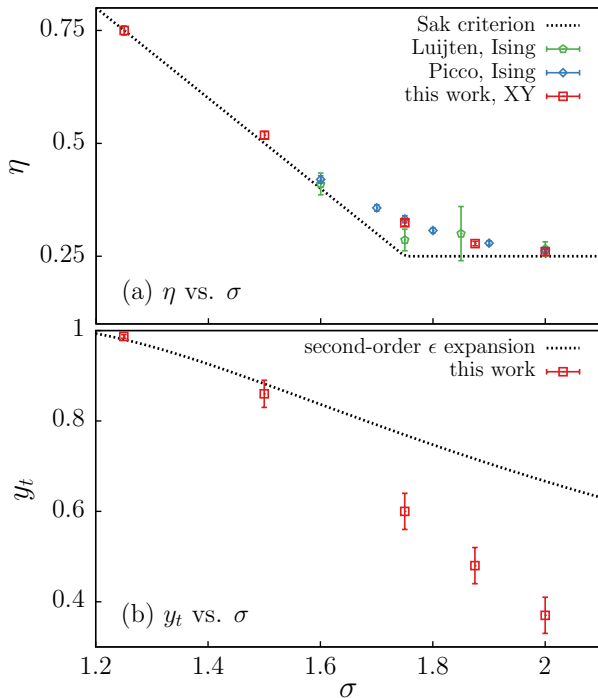


FIG. 17. The value of critical exponent at various  $\sigma$ . (a) The red dots denote the estimates of  $\eta$  in this work. Picco and Luijten’s results are also contained [8, 11], respectively denoted by blue and green dots. Although the model they studied is the Ising model, our estimated values of  $\eta$  are consistent with their results. The dotted lines correspond to Sak’s prediction:  $\eta = \max(2 - \sigma, \frac{1}{4})$ . Obviously, our results deviate from Sak’s prediction, suggesting that for  $1.75 < \sigma < 2$ , the short-range behavior is not recovered. (b) The red dots denote the estimates of  $y_t$  in this work. The dotted line represents the results from second-order  $\epsilon$  expansion [2] (note that  $y_t = 1/\nu$ ).

responding to the estimated value of exponents finally converge to a plateau, indicating the reliability of the fitting results. Figure 17 presents our numerical estimates of critical exponents at different  $\sigma$ . Panel (a) displays our estimates for  $\eta$  across different  $\sigma$  values, alongside the estimates by Picco[11] and Luijten[8]. Despite the difference in models (Luijten and Picco studied the 2D LR Ising model, whereas we are studying the 2D LR XY model), our results are consistent with Picco’s, which does not agree with Sak’s prediction. In our results,  $\eta$  interpolates smoothly between  $\eta = 2 - \sigma$  for  $\sigma$  near 1 and  $\eta = \eta_{SR} = \frac{1}{4}$  for  $\sigma > 2$ . For  $\sigma < 2$ ,  $\eta$  remains significantly higher than  $\frac{1}{4}$ , indicating the phase transition doesn’t belong to the short-range universality class. For  $\sigma = 2$ , the estimated value of  $\eta$  still slightly exceeds  $\frac{1}{4}$ , which could be attributed to some logarithmic corrections in the behavior of  $\chi$  at the marginal point  $\sigma = 2$ . As mentioned before, Ref. [9] suggests that Picco might underestimate the finite-size correction, which finally caused the overestimate of  $\eta$ , and by studying the short-distance correction to the correlation function, they

proposed that when properly considering the finite-size correction term,  $\eta$  would revert to 0.25 at  $\sigma = 1.75$ , consistent with Sak’s criterion. Inspired by Ref. [9], we also check our estimate of  $\eta$  at  $\sigma = 1.75$  following the same method by studying the correlation function. The analysis is conducted in the next subsection, and our estimate of  $\eta$  is found to be reliable. Panel (b) in Fig. 17 demonstrates our numerical estimates of  $y_t$ , as well as the  $\epsilon$  expansion, which results up to the second order [2]. As  $\sigma$  approaches 2, the numerical estimates of  $y_t$  gradually deviate from the results of the  $\epsilon$ -expansion.

### C. Subleading Magnetic Exponents

Strong correction to correlation functions  $g(r)$  has been observed in the 2D LR Ising model, and the neglect of such corrections could lead to an overestimate of  $\eta$  [9]. In this part, following the same routine in Ref. [9], we study the correlation function at the critical point for the 2D LR XY model. In particular, we focus on the case of  $\sigma = 1.75$  where  $\eta$  is estimated to be 0.324(7), and similar procedures can apply to other  $\sigma$ . Our estimated value of  $\eta$  is taken to be 0.32, with the corresponding correction exponent  $\omega$  in Eq. (41) being 0.45. By carefully fitting the correlation function, we identify a subleading power-law correction likely arising from the subleading magnetic exponent  $y_{h,2}$  of the transition [37]. The fitting results are compatible with our estimates of  $\eta$ , thus validating our previous analysis.

The two-point correlation function is defined as  $g(r) = \langle \mathbf{S}(0) \cdot \mathbf{S}(r) \rangle$ , and at the critical point, it asymptotically decays as a power of the separation,  $g(r) \propto r^{-\eta}$  as  $r \rightarrow \infty$ . However, one would expect additional corrections to  $g(r)$  that decay faster than the leading term. These corrections are, in general, difficult to observe in SR models. It is argued in Ref. [9] that  $g(r)$  in the LR Ising model at the criticality is controlled by two power-law decays, as  $g(r) = r^{-\eta}(a + br^{-\delta})$ . The term  $r^{-\delta}$  causes faster decay in short distances and reduces to 0 at large  $r$  when the correlation function gradually returns to the single power scaling, i.e.,  $r^{-\eta}$ . Such correction, if not properly considered, could lead to an unreliable estimation of  $\eta$  [9].

We measure the correlation function in horizontal and vertical axes:

$$g(r) = \frac{1}{2N_s} \sum_{\langle i,j \rangle \in \{N_s\}} (\langle \mathbf{S}_{i,j} \cdot \mathbf{S}_{i+r,j} \rangle + \langle \mathbf{S}_{i,j} \cdot \mathbf{S}_{i,j+r} \rangle), \quad (43)$$

where the summation only goes through  $N_s$  randomly chosen sites instead of the entirety, and  $N_s = 100$  in our practice. In this way, the complexity of this measurement remains  $O(N)$  instead of  $O(N^2)$ , which allows us to measure the system with a larger size and simulate more samples. The cost is the slightly higher uncertainty in the measurement, but this can be compensated by involving more samples.

TABLE VI. fitting detail of  $\chi$  to Eq. (41) for various  $\sigma$ .

$\sigma$	$L_{\min}$	$\eta$	$c$	$a$	$b$	$\omega$	$\chi^2/\text{DF}$
1.25	8	0.742(3)	-0.92(6)	0.64(1)	1.04(3)	0.4	8.5/10
	16	0.742(4)	-1.0(2)	0.63(2)	1.05(5)		8.5/9
	8	0.758(2)	-1.39(9)	0.74(1)	1.18(4)	0.5	11.8/10
	16	0.755(3)	-1.7(3)	0.73(2)	1.24(7)		10.2/9
1.5	32	0.511(4)	3.0(7)	0.50(2)	0.51(5)	0.4	9.8/8
	48	0.517(5)	5(2)	0.52(3)	0.42(8)		7.6/7
	16	0.525(1)	-1.2(3)	0.568(6)	1.22(5)	0.7	10.0/9
	32	0.526(2)	-0.2(10)	0.575(9)	1.1(1)		8.7/8
1.75	16	0.3169(7)	1.6(1)	0.363(2)	0.535(6)	0.4	7.0/11
	32	0.3164(9)	1.3(4)	0.362(3)	0.541(9)		6.6/10
	32	0.3305(7)	-3.5(6)	0.422(2)	0.91(2)	0.6	10.1/10
	48	0.3298(8)	-5(1)	0.419(3)	0.94(3)		8.4/9
1.875	48	0.273(1)	3.8(7)	0.386(4)	0.41(1)	0.35	9.7/10
	64	0.274(1)	5(1)	0.388(5)	0.40(1)		8.8/9
	16	0.2814(5)	1.0(1)	0.425(2)	0.491(6)	0.45	11.7/12
	32	0.2812(7)	0.9(4)	0.424(2)	0.494(10)		11.6/11
2	48	0.2559(7)	5.2(6)	0.465(3)	0.299(9)	0.35	10.5/10
	64	0.2562(8)	6(1)	0.466(4)	0.29(1)		10.0/9
	32	0.2645(2)	-0.6(3)	0.5131(9)	0.555(8)	0.6	5.6/11
	48	0.2643(3)	-1.2(6)	0.512(1)	0.56(1)		5.0/10

TABLE VII. fitting detail of  $K$  to Eq. (42) for various  $\sigma$ .

$\sigma$	$L_{\min}$	$y_t$	$a$	$b$	$\omega$	$\chi^2/\text{DF}$
1.25	8	0.991(2)	0.444(5)	0.067(8)	0.4	8.2/11
	16	0.989(2)	0.453(7)	0.05(1)		6.2/10
	8	0.9833(6)	0.473(1)	0.56(7)	2	8.4/11
	16	0.9839(7)	0.472(2)	0.9(3)		7.4/10
1.5	8	0.830(2)	1.60(3)	-1.21(4)	0.1	9.3/10
	16	0.826(3)	1.67(5)	-1.29(6)		7.4/9
	16	0.886(2)	0.69(1)	-0.43(3)	0.5	10.8/9
	32	0.883(3)	0.71(2)	-0.49(6)		9.3/8
1.75	32	0.558(4)	5.1(2)	-5.1(2)	0.1	11.8/11
	48	0.553(5)	5.4(3)	-5.5(3)		9.5/10
	48	0.640(3)	1.48(3)	-3.3(2)	0.6	9.4/10
	64	0.640(4)	1.48(4)	-3.3(3)		9.4/9
1.875	16	0.441(2)	6.9(1)	-7.1(1)	0.1	10.8/12
	32	0.439(3)	7.0(2)	-7.3(3)		10.2/11
	48	0.518(3)	2.04(4)	-3.9(2)	0.5	8.6/10
	64	0.518(4)	2.04(6)	-3.9(3)		8.6/9
2	32	0.337(3)	8.9(3)	-9.6(3)	0.1	9.7/11
	48	0.332(4)	9.3(4)	-10.2(5)		7.6/10
	64	0.416(4)	2.53(7)	-5.6(3)	0.5	6.9/9
	128	0.411(6)	2.6(1)	-6.3(8)		5.4/7

The left panel in Fig. 18 demonstrates the correlation function in various  $L$  where the double-log scale is used to observe the power-law behavior. The inset shows the curves of the correlation function with the x-axis being distance  $r$ . It can be observed that curves flatten in their tails near  $L/2$  due to the finite-size effect. To diminish the effect and for a better observation of the power-law behavior, we follow the treatment of Ref. [9] to choose the x-axis as  $\sin(\pi r/L)L/\pi$  in the main figure. It does not affect the correlation function in short distances since  $\sin(\pi r/L)L/\pi \approx (\pi r/L)L/\pi = r$ . Moreover, as can be seen in the main figure, it drastically reduces the bound-

ary effect. In both the inset and the main figure,  $g(r)$  exhibits a fast decay in the short distance and then decays slowly as  $r$  increases, which suggests an additional correction to the correlation function. We then perform a detailed fit to the correlation function of the largest system size  $L = 4096$  with  $\eta$  fixed at 0.32:

$$g(r) = r'^{-\eta}(a + br'^{-\delta}), \quad (44)$$

where  $r' = \sin(\pi r/L)L/\pi$ . We use data ranging from  $r = 1$  to 600 for fitting, minimizing the impact of boundary effects. The fit results in a corresponding  $\delta$  value of 0.42. The right panel in Fig. 18 visually shows the quality of

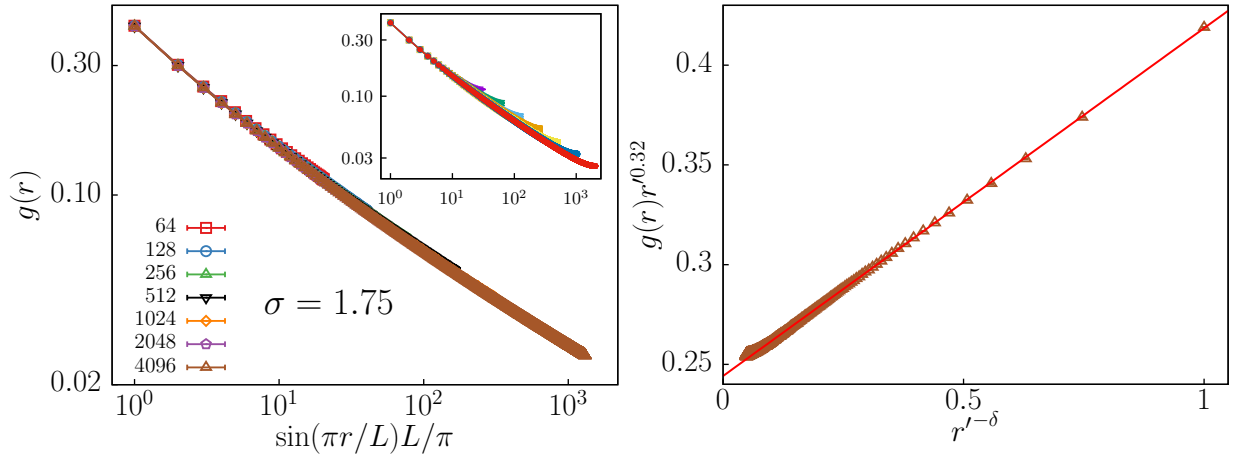


FIG. 18. (Left) The correlation function  $g(r)$  for systems of different sizes is plotted for  $\sigma = 1.75$ . Both the main figure and inset are shown in double-logarithmic coordinates for convenient observation of the power-law behavior. In the inset, with the x-axis representing  $r$ , the correlation function curves exhibit a strong boundary effect, i.e., a noticeable tendency to bend upwards as  $r$  approaches  $L/2$ . In the main figure, the x-axis is replaced by  $\sin(\pi r/L)L/\pi$  to reduce this boundary effect. Furthermore, in this representation, the behavior of the correlation function at short distances remains unaffected. (Right) Rescaled correlation function  $g(r)r'^{\eta}$  versus  $r'^{-\delta}$  for  $L = 4096$ , with  $\eta = 0.32$  and  $\delta = 0.42$ . The red line represents the fitted line. This figure visually demonstrates the contribution of the subleading magnetic exponent to  $g(r)$  (discussed in the text).

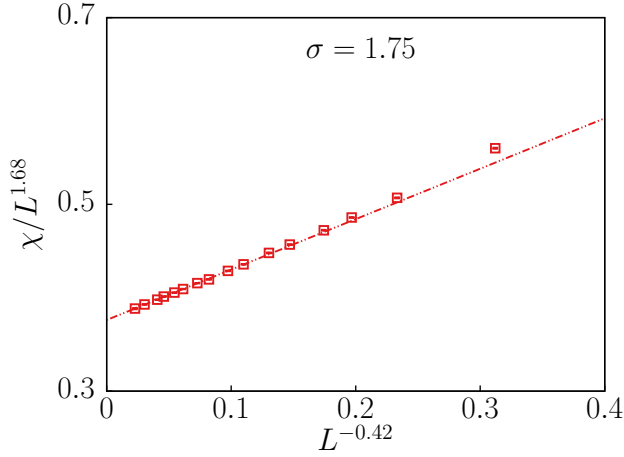


FIG. 19. The plot of  $\chi/L^{2-\eta}$  versus  $L^{-\delta}$  for  $\sigma = 1.75$ , where  $\eta = 0.32$  and the corresponding  $\delta = 0.42$ , obtained from the fitting of Eq. (44). As the system size  $L \rightarrow \infty$ , the red dots approach a straight line, indicating the scaling behavior:  $\chi \sim L^{2-\eta}(a + b \cdot L^{-\delta})$  with  $\eta = 0.32$  and  $\delta = 0.42$ . This shows the consistency between the fitting of  $\chi$  and  $g(r)$ .

fitting, where the x and y-axis are respectively  $r'^{-\delta}$  and  $g(r)r'^{\eta}$ , and thus the data points should approximately form a straight line according to Eq. (44). As shown in the figure, the data points fit well with a straight line and are only slightly flattened at large distances due to the boundary effect. Therefore, the fitting of the correlation function is compatible with  $\eta = 0.32$ .

We also demonstrate that the correction to correlation has been properly included in the fitting of  $\chi$ . It is argued in Ref. [9] that Picco did not sufficiently account for the

finite-size corrections deriving from the second term in the double power of the correlation function, leading to an overestimation of  $\eta$ . Hence, we compare the value of correction exponent  $\omega$  considered in the fitting of  $\chi$  using Eq. (41), and of the second exponent  $\delta$  in Eq. (44). For  $\eta = 0.32$ , the corresponding  $\omega$  in the fit of Eq. (41) is approximately 0.45, while the fit of Eq. (44) gives a  $\delta$  of 0.42. Since these values are very close, we believe that the correction term  $bL^{-\omega}$  in Eq. (41) has already accounted for the subleading term  $r'^{-\delta}$  of the correlation function. Figure. 19 plots  $\chi/L^{2-\eta}$  as a function of  $L^{-\delta}$  with  $\eta = 0.32$  and  $\delta = 0.42$ , where the data points asymptotically follows a linear behavior. This suggests that  $\chi$  indeed scales as  $\sim L^{2-\eta}(a + b \cdot L^{-\delta})$  and our previous estimate of  $\eta$  by fitting  $\chi$  is reliable.

The additional power-law correction to  $g(r)$  should originate from a subleading relevant magnetic scaling field. In the context of RG, the free-energy density depends on not only the leading thermal and magnetic scaling fields  $t_1 \equiv t$ ,  $h_1 \equiv h$  but rather a full set of scaling fields. Each scaling field is associated with a particular eigenvalue of the RG transformation. In particular, the subleading thermal and magnetic scaling fields  $t_2$  and  $h_2$  correspond to the subleading eigenvalues in the even sector and odd sector, respectively. The contributions of these subleading exponents are very difficult to observe explicitly from numerical simulations because they either decay very fast or have very small, even zero amplitude. For instance, for the NN Ising model, one has  $y_{t,2} = -4/3$  and  $y_{h,2} = 13/24 \approx 0.542$  [54]. The subleading thermal field  $t_2$  is irrelevant, whose contribution to FSS decays quickly. As for the subleading magnetic field  $h_2$ , despite being relevant, it is commonly believed to be

redundant [55, 56]. To our knowledge, direct numerical evidence for  $y_{h,2}$  remains obscure.

Taking into account the dependence on the additional magnetic scaling field  $h_2$ , the singular part of free energy density for a finite system near criticality scales as  $f \sim L^{-d} f(t_1 L^{y_{t,1}}, h_1 L^{y_{h,1}}, h_2 L^{y_{h,2}}, \dots)$ , where  $y_{t,1} \equiv y_t$ ,  $y_{h,1} \equiv y_h$ , and  $y_{h,2}$  are the corresponding scaling exponents. Consequently, at critical point  $t = 0$ , the correlation function  $g(r)$ , acquires additional power-law terms as  $g(r) \sim g_0 r^{2y_{h,1}-2d} + g_1 r^{y_{h,1}+y_{h,2}-2d} + g_2 r^{2y_{h,2}-2d}$  [37]. From our fitting, the anomalous dimension of the sub-leading power-law decay is  $\eta' \equiv \eta + \delta = 0.74$ . Therefore, if this exponent is from the  $r^{y_{h,1}+y_{h,2}-2d}$  term, one has  $y_{h,2} = 2 - (\eta' - \eta/2) \approx 1.42$ ; or, if it is from  $r^{2y_{h,2}-2d}$ , then  $y_{h,2} = 2 - \eta'/2 \approx 1.63$ . Either case is possible, though, from a symmetry consideration, we believe the latter case is more likely. Nonetheless, one could conclude that the correction to  $g(r)$  is most likely due to  $y_{h,2}$ .

We are grateful to observe the contribution of the sub-leading magnetic field at criticality in the LR XY model, which is difficult to identify numerically in previous studies of SR cases. In our opinion, this strong correction to  $g(r)$  is another piece of evidence that the system is not in the SR universality class at  $\sigma = 1.75$ . Note that the double power correlation function observed in the LR Ising model could also be attributed to the contribution of  $y_{h,2}$ , suggesting a different universality class than the SR one at  $\sigma = 1.75$ .

## VII. CONCLUSION

In this study, we have extended our previous work [19] to provide a comprehensive understanding of the two-dimensional long-range (LR) XY model with algebraically decaying interactions. We conduct large-scale Monte Carlo simulations to study the low- $T$ , high- $T$ , and critical properties of the model at various  $\sigma$ . We present strong evidence that the threshold between long-range and short-range universality lies at  $\sigma_* = 2$ , which contrasts Sak's scenario [57] and previous theoretical predictions [17, 18].

We show that for  $\sigma \leq 2$ , the system exhibits long-range order and Goldstone mode excitations in the low- $T$  phase, while for  $\sigma > 2$ , the system enters a QLRO phase via a BKT transition, belonging to the SR universality. Furthermore, we reveal the distinct growth behaviors of the correlation length  $\xi$  in the high- $T$  phase as the system approaches  $T_c$ . For  $\sigma \leq 2$ , the correlation length follows a power-law divergence, indicative of a second-order transition; for  $\sigma > 2$ , the typical exponential growth of the BKT transition is observed. Finally, we determine the critical points and critical exponents of the model in the regime  $1 < \sigma \leq 2$ . The resulting phase diagram highlights the different universality classes for  $\sigma \leq 2$  and  $\sigma > 2$ , providing deeper insights into the phase transitions in long-range interacting systems.

The findings presented in this work significantly enhance our understanding of the crossover between short-range and long-range interactions in the two-dimensional XY model. This crossover is crucial for elucidating the impact of long-range interactions in experimental systems, such as Rydberg atom arrays, where tunable interactions are prevalent. Moreover, our study provides valuable insights into how the nature of these interactions influences phase behavior and critical phenomena, offering broader implications for the fields of statistical mechanics, condensed matter physics, and cold atom physics. This work also lays the groundwork for future research into systems with long-range interactions, like the long-ranged Ising model and Heisenberg model, as well as the self-avoiding walk.

## ACKNOWLEDGEMENTS

We acknowledge the support by the National Natural Science Foundation of China (NSFC) under Grant No. 12204173 and No. 12275263, as well as the Innovation Program for Quantum Science and Technology (under Grant No. 2021ZD0301900). YD is also supported by the Natural Science Foundation of Fujian Province 802 of China (Grant No. 2023J02032).

- 
- [1] F. J. Dyson, *Communications in Mathematical Physics* **12**, 91 (1969).
  - [2] M. E. Fisher, S.-k. Ma, and B. G. Nickel, *Physical Review Letters* **29**, 917 (1972).
  - [3] J. M. Kosterlitz, *Reviews of Modern Physics* **89**, 040501 (2017).
  - [4] E. Luijten and H. Meßingfeld, *Physical Review Letters* **86**, 5305 (2001).
  - [5] J. Honkonen and M. Y. Nalimov, *Journal of Physics A: Mathematical and General* **22**, 751 (1989).
  - [6] J. Honkonen, *Journal of Physics A: Mathematical and General* **23**, 825 (1990).
  - [7] N. Defenu, A. Trombettoni, and A. Codello, *Physical Review E* **92**, 052113 (2015).
  - [8] E. Luijten and H. W. J. Blöte, *Physical Review Letters* **89**, 025703 (2002).
  - [9] M. C. Angelini, G. Parisi, and F. Ricci-Tersenghi, *Physical Review E* **89**, 062120 (2014).
  - [10] T. Horita, H. Suwa, and S. Todo, *Physical Review E* **95**, 012143 (2017).
  - [11] M. Picco, Critical behavior of the Ising model with long range interactions (2012), arXiv:1207.1018 [cond-mat, physics:hep-th].
  - [12] T. Blanchard, M. Picco, and M. A. Rajabpour, *Europhysics Letters* **101**, 56003 (2013).

- [13] P. Grassberger, *Journal of Statistical Physics* **153**, 289 (2013).
- [14] M. I. Berganza and L. Leuzzi, *Physical Review B* **88**, 144104 (2013).
- [15] J. Zhao, M. Song, Y. Qi, J. Rong, and Z. Y. Meng, *npj Quantum Materials* **8**, 59 (2023).
- [16] F. Cescatti, M. Ibáñez-Berganza, A. Vezzani, and R. Burioni, *Physical Review B* **100**, 054203 (2019).
- [17] G. Giachetti, N. Defenu, S. Ruffo, and A. Trombettoni, *Physical Review Letters* **127**, 156801 (2021).
- [18] G. Giachetti, A. Trombettoni, S. Ruffo, and N. Defenu, *Physical Review B* **106**, 014106 (2022).
- [19] T. Xiao, D. Yao, C. Zhang, Z. Fan, and Y. Deng, *arxiv* 10.48550/arXiv.2404.08498 (2024), [arXiv:2404.08498](https://arxiv.org/abs/2404.08498) [cond-mat.stat-mech].
- [20] M. Aizenman and B. Simon, *Physics Letters A* **76**, 281 (1980).
- [21] K. Kirkpatrick and T. Nawaz, *Journal of Statistical Physics* **165**, 1114 (2016).
- [22] K. Kirkpatrick and T. Nawaz, in *Stochastic Analysis and Related Topics*, Vol. 72, edited by F. Baudoin and J. Peterson (Springer International Publishing, Cham, 2017) pp. 207–221.
- [23] D. Frenkel and B. Smit, *Understanding Molecular Simulation: From Algorithms to Applications*, 2nd ed., Computational Science Series No. Volume 1 (Academic press, San Diego, 2002).
- [24] W. Janke, H. Christiansen, and S. Majumder, *Journal of Physics: Conference Series* **1163**, 012002 (2019).
- [25] R. Agrawal, F. Corberi, E. Lippiello, P. Politi, and S. Puri, *Physical Review E* **103**, 012108 (2021).
- [26] M. Michel, X. Tan, and Y. Deng, *Physical Review E: Statistical Physics, Plasmas, Fluids, and Related Interdisciplinary Topics* **99**, 010105 (2019).
- [27] R. H. Swendsen and J.-S. Wang, *Physical Review Letters* **58**, 86 (1987).
- [28] U. Wolff, *Physical Review Letters* **62**, 361 (1989).
- [29] O. F. Syljuåsen and A. W. Sandvik, *Physical Review E* **66**, 046701 (2002).
- [30] N. Prokof'ev and B. Svistunov, *Physical Review Letters* **87**, 160601 (2001).
- [31] M. Boninsegni, N. V. Prokof'ev, and B. V. Svistunov, *Physical Review E: Statistical Physics, Plasmas, Fluids, and Related Interdisciplinary Topics* **74**, 036701 (2006).
- [32] E. Luijten and H. W. Blöte, *International Journal of Modern Physics C (IJMPC)* **06**, 359 (1995).
- [33] K. Fukui and S. Todo, *Journal of Computational Physics* **228**, 2629 (2009), [arXiv:0802.0272](https://arxiv.org/abs/0802.0272) [cond-mat].
- [34] Z. Fan, C. Zhang, and Y. Deng, *arxiv* <https://arxiv.org/abs/2305.14082> (2023), [arXiv:2305.14082](https://arxiv.org/abs/2305.14082).
- [35] M. Michel, S. C. Kapfer, and W. Krauth, *The Journal of Chemical Physics* **140**, 054116 (2014), [arXiv:1309.7748](https://arxiv.org/abs/1309.7748) [cond-mat].
- [36] E. Luijten and H. W. J. Blöte, *Physical Review B* **56**, 8945 (1997).
- [37] H. W. J. Blöte, E. Luijten, and J. R. Heringa, *Journal of Physics A: Mathematical and General* **28**, 6289 (1995).
- [38] J. Salas and A. D. Sokal, *Journal of Statistical Physics* **92**, 729 (1998).
- [39] S. Caracciolo, R. G. Edwards, A. Pelissetto, and A. D. Sokal, *Nuclear Physics B* **403**, 475 (1993).
- [40] L. M. Tuan, T. T. Long, D. X. Nui, P. T. Minh, N. D. Trung Kien, and D. X. Viet, *Physical Review E* **106**, 034138 (2022).
- [41] R. G. Edwards and A. D. Sokal, *Physical Review. D, Particles and Fields* **40**, 1374 (1989).
- [42] D. X. Viet and H. Kawamura, *Physical Review B* **80**, 064418 (2009).
- [43] C. Ding, W. Guo, and Y. Deng, *Physical Review B* **90**, 134420 (2014).
- [44] Y. Deng and H. W. J. Blöte, *Physical Review E* **68**, 036125 (2003).
- [45] Y. Komura and Y. Okabe, *Computer Physics Communications* **183**, 1155 (2012), [arXiv:1202.0635](https://arxiv.org/abs/1202.0635) [cond-mat, physics.physics].
- [46] N. Defenu, T. Donner, T. Macrì, G. Pagano, S. Ruffo, and A. Trombettoni, *Reviews of Modern Physics* **95**, 035002 (2023).
- [47] M. Kardar, *Statistical Physics of Fields* (Cambridge University Press, Cambridge, 2007).
- [48] Y. Komura and Y. Okabe, *Journal of the Physical Society of Japan* **81**, 113001 (2012).
- [49] J. M. Kosterlitz and D. J. Thouless, *Journal of Physics C: Solid State Physics* **6**, 1181 (1973).
- [50] J. M. Kosterlitz, *Journal of Physics C: Solid State Physics* **7**, 1046 (1974).
- [51] Y. Kumano, K. Hukushima, Y. Tomita, and M. Oshikawa, *Phys. Rev. B* **88**, 104427 (2013).
- [52] K. Harada and N. Kawashima, *Phys. Rev. B* **55**, R11949 (1997).
- [53] B.-Z. Wang, P. Hou, C.-J. Huang, and Y. Deng, *Physical Review E* **103**, 062131 (2021).
- [54] C. Domb, M. S. Green, and J. L. Lebowitz, eds., *Phase Transitions and Critical Phenomena. Vol. 11*, Vol. 11 (Acad. Press, London, 1987).
- [55] H. Blöte, A. Compagner, J. Croockewit, Y. Fonk, J. Heringa, A. Hoogland, T. Smit, and A. Van Willigen, *Physica A: Statistical Mechanics and its Applications* **161**, 1 (1989).
- [56] C. F. Baillie, R. Gupta, K. A. Hawick, and G. S. Pawley, *Physical Review B* **45**, 10438 (1992).
- [57] J. Sak, *Physical Review B* **8**, 281 (1973).